MIGHTEE-HI: the radial acceleration relation with resolved stellar mass measurements

Andreea A. Vărăşteanu,[1]⋆ Matt J. Jarvis [1,2] Anastasia A. Ponomareva [1,3] Harry Desmond [4]
Ian Heywood,[1,5,6] Tariq Yasin [1] Natasha Maddox [7] Marcin Glowacki,[8,9]
Michalina Maksymowicz-Maciata,[7] Pavel E. Mancera Piña [10] and Hengxing Pan [11]

[1]*Oxford Astrophysics, Denys Wilkinson Building, University of Oxford, Keble Road, Oxford OX1 3RH, UK*
[2]*Department of Physics and Astronomy, University of the Western Cape, Robert Sobukwe Road, 7535 Bellville, Cape Town, South Africa*
[3]*Centre for Astrophysics Research, School of Physics, Astronomy and Mathematics, University of Hertfordshire, College Lane, Hatfield AL10 9AB, UK*
[4]*Institute of Cosmology and Gravitation, University of Portsmouth, Dennis Sciama Building, Portsmouth PO1 3FX, UK*
[5]*Centre for Radio Astronomy Techniques and Technologies, Department of Physics and Electronics, Rhodes University, PO Box 94, Makhanda 6140, South Africa*
[6]*South African Radio Astronomy Observatory, 2 Fir Street, Black River Park, Observatory, Cape Town 7925, South Africa*
[7]*School of Physics, H.H. Wills Physics Laboratory, Tyndall Avenue, University of Bristol, Bristol BS8 1TL, UK*
[8]*Institute for Astronomy, University of Edinburgh, Royal Observatory, Edinburgh EH9 3HJ, UK*
[9]*Inter-University Institute for Data Intensive Astronomy, Department of Astronomy, University of Cape Town, Cape Town, South Africa*
[10]*Leiden Observatory, Leiden University, P.O. Box 9513, NL-2300 RA Leiden, the Netherlands*
[11]*National Astronomical Observatories, Chinese Academy of Sciences, Beijing 100101, People's Republic of China*

ABSTRACT
The radial acceleration relation (RAR) is a fundamental relation linking baryonic and dark matter in galaxies by relating the observed acceleration derived from dynamics to the one estimated from the baryonic mass. This relation exhibits small scatter, thus providing key constraints for models of galaxy formation and evolution – allowing us to map the distribution of dark matter in galaxies – as well as models of modified dynamics. However, it has only been extensively studied in the very local Universe with largely heterogeneous samples. We present a new measurement of the RAR, utilizing a homogeneous sample of 19 H I-selected galaxies out to $z = 0.08$. We introduce a novel approach of measuring resolved stellar masses using spectral energy distribution fitting across 10 photometric bands to determine the resolved mass-to-light ratio, which we show is essential for measuring the acceleration due to baryons in the low-acceleration regime. Our results reveal a tight RAR with a low-acceleration power-law slope of ~ 0.5, consistent with previous studies. Adopting a spatially varying mass-to-light ratio yields the tightest RAR with an intrinsic scatter of only 0.045 ± 0.022 dex, highlighting the importance of resolved stellar mass measurements in accurately characterizing the gravitational contribution of the baryons in low-mass, gas-rich galaxies. We also find the first tentative evidence for redshift evolution in the acceleration scale, but more data will be required to confirm this. Adopting a more general MOND interpolating function, we find that our results ameliorate the tension between previous RAR analyses, the Solar System quadrupole, and wide-binary test.

Key words: galaxies: formation – galaxies: fundamental parameters – galaxies: kinematics and dynamics – dark matter.

1 INTRODUCTION

The missing gravity problem, highlighted by the flatness of rotation curves, arises from observations of galaxies that reveal a discrepancy between the visible matter (stars, gas, and dust) and the dynamical one (van den Bergh 2001; McGaugh 2004). According to Newtonian dynamics, the rotational velocity of stars and gas in a galaxy should decrease with distance from the centre. However, observations reveal that they remain fairly constant (Bosma 1978; Rubin, Ford & Thonnard 1978), implying the presence of an unseen mass component, known as dark matter, that dominates the outer regions of galaxies. This observation is a key motivation for the ΛCDM model, the current cosmological paradigm, in which galaxies form and evolve within massive dark-matter haloes. This framework successfully explains the large-scale structure in the Universe. However, it faces several challenges on smaller scales, particularly in relation to galaxy dynamics, where discrepancies arise (see Bullock & Boylan-Kolchin 2017, for a review). Examples include the cusp-core problem (Flores & Primack 1994; Moore 1994), the missing satellites problem (Klypin et al. 1999; Moore et al. 1999), and the too-big-to-fail problem (Boylan-Kolchin, Bullock & Kaplinghat 2011, 2012; Garrison-Kimmel et al. 2013; Verbeke et al. 2017).

Some of the most intriguing aspects of galaxy dynamics in this framework are the tight scaling relations between baryonic properties and the dynamics of galaxies. A well-known example is the

⋆ E-mail: andreea.varasteanu@physics.ox.ac.uk

Tully–Fisher Relation (TFR; Tully & Fisher 1977) that links the luminosity of a galaxy to the width of its global H I profile, or its extended form, the baryonic Tully–Fisher Relation (bTFR), which links the baryonic mass (stars and gas) to the flat rotation velocity of the galaxy, spanning over 5 dex in baryonic mass (McGaugh et al. 2000; McGaugh 2012; Lelli et al. 2019; Ponomareva et al. 2018, 2021).

The radial acceleration relation (RAR) generalizes the bTFR by connecting the local observed dynamics of galaxies to the mass distribution within them across the full extent of galaxies. Previously termed the mass discrepancy–acceleration relation (Sanders 1990; McGaugh 2004), the RAR as such was first reported by McGaugh, Lelli & Schombert (2016) using the SPARC data base (Spitzer Photometry and Accurate Rotation Curves), consisting of 175 late-type galaxies with accurate H I rotation curves (Lelli, McGaugh & Schombert 2016). The RAR is a remarkably tight empirical correlation between the observed radial acceleration (g_{obs}), derived from rotation curves (thus including both baryonic and dark matter in the ΛCDM paradigm) and the one derived solely from the distribution of baryons (g_{bar}). The RAR suggests that the distribution of dark matter is closely tied to the distribution of visible matter, with minimal scatter, largely driven by observational uncertainties (Lelli et al. 2017).

The high acceleration end of this relation corresponds to baryon-dominated regions in massive galaxies. Here, the RAR follows a one-to-one relation (Desmond, Bartlett & Ferreira 2023), which implies that the observed dynamics can be fully accounted for by baryons alone. However, at lower accelerations, below a certain characteristic acceleration scale of $\approx 10^{-10}$ m s^{-2} (McGaugh et al. 2016; Lelli et al. 2017), the observed dynamics deviates significantly from what we infer from baryons alone, and this is generally attributed to the influence of dark matter. The inner parts of massive galaxies contribute to the high acceleration portion of the RAR, whereas the outer parts of high-mass galaxies and all regions of low-mass galaxies contribute to the lower acceleration regime. Such an intimate baryon-dark matter coupling is not trivially expected in a ΛCDM cosmology, where galaxies form and evolve via stochastic processes (e.g. hot and cold mode gas accretion to dark matter haloes, supernova, and AGN feedback), which should naturally introduce substantial scatter, particularly at the low-mass end of the galaxy population, where dark matter dominates.

However, the RAR shows remarkably low scatter, potentially even consistent with zero (Lelli et al. 2017), making it the tightest known dynamical galaxy scaling relation (Desmond 2023). This makes it a powerful diagnostic tool to provide key insights into the elusive nature of dark matter, by enabling us to impose stringent observational constraints on galaxy formation models (Desmond 2017). Any successful theoretical framework must be able to reproduce this tight relation across a wide range of galaxy types and masses. This stringent requirement has been used by some to argue for Modified Newtonian Dynamics (MOND; Milgrom 1983; Sanders 1990) as an alternative to ΛCDM, which produces the relation more naturally (e.g. Lelli et al. 2017).

The RAR has been studied extensively at redshift $z \approx 0$ for various galaxy samples, from rotationally supported galaxies (spirals and irregulars) to local dwarf spheroidals and pressure-supported early-type galaxies (ETGs), even extending to weak lensing-based studies (Lelli et al. 2017; Brouwer et al. 2021; Mistele et al. 2024). This has also been extended to $z \approx 0.02$ with ultra-diffuse galaxies in clusters (Freundlich et al. 2022) and galaxy groups and clusters (Chan & Del Popolo 2020; Tian et al. 2020, 2024). It is important to note that accurately measuring g_{bar} and g_{obs} is dependent on knowledge of their true

distance, inclination and mass-to-light ratio, but they are often considered nuisance parameters in RAR studies (e.g. Desmond 2023).

Much of the work to measure and understand the RAR using the SPARC galaxies, have either fixed their mass-to-light ratios (Lelli et al. 2017) or varied these 'nuisance parameters' when fitting the RAR galaxy-by-galaxy with a functional form (Li et al. 2018; Chae et al. 2020, 2021, 2022), finding a small intrinsic scatter (< 0.1 dex). On the other hand, Desmond (2023) performed a full joint inference to map the degeneracies between all parameters and infer the acceleration scale with or without an external field effect (EFE), to find an intrinsic scatter of 0.034 ± 0.001 (statistical) ± 0.001 (systematic). Furthermore, Stiskalek & Desmond (2023) show that the RAR satisfies all postulated criteria for a unique fundamental 1D correlation that governs the radial dynamics in late-type galaxies, with all other dynamical scaling relations being nothing more than projections of the RAR.

The observed RAR has motivated numerous efforts to reproduce it within the standard ΛCDM framework using both cosmological hydrodynamical simulations (e.g. Keller & Wadsley 2017; Ludlow et al. 2017; Garaldi et al. 2018; Tenneti et al. 2018; Dutton et al. 2019; Mercado et al. 2024) and semi-analytic models (e.g. Desmond 2017; Navarro et al. 2017). While some studies have successfully recovered a tight relation similar to that observed (Keller & Wadsley 2017; Paranjape & Sheth 2021), they often show significant differences in the inferred acceleration scale or intrinsic scatter compared to SPARC studies (Ludlow et al. 2017; Tenneti et al. 2018). For instance, Keller & Wadsley (2017) found agreement with the SPARC RAR, though their results were limited by sample size. Conversely, Ludlow et al. (2017) (EAGLE simulation) and Tenneti et al. (2018) (MassiveBlack-II simulation) reported acceleration scales substantially larger than obtained with SPARC, and the latter also a power-law form that is not consistent with the observations. More recently, Paranjape & Sheth (2021) showed the RAR could emerge naturally from baryonic processes without fine-tuning, with predicted deviations from the MOND-inspired RAR at extremely low accelerations. In parallel, observational probes at large radii using weak lensing techniques in isolated Milky Way size galaxies also yielded mixed results (Brouwer et al. 2021), due to the omission/inclusion of hot, ionized gas component in the baryonic budget. The agreement of the weak lensing of the RAR with the SPARC one was however much improved by the updated analysis of Mistele et al. (2024). Altogether, these results highlight the ongoing challenges in reproducing the observed RAR within ΛCDM.

To investigate the RAR, one needs photometric observations that trace the baryonic mass, coupled with spectroscopic information to determine the dynamical mass. Atomic hydrogen, emitted at 21 cm, is particularly important for determining the rotation curves of galaxies because it is dynamically cold, with a low velocity dispersion compared to the overall rotational velocity and extends far beyond the stellar disc, out to the large radii where dark matter is expected to dominate. Other emission lines such as CO (Topal et al. 2018) or Hα (Tiley et al. 2016; Übler et al. 2017) can be used at higher redshifts but they only trace the central mass distribution and do not extend beyond the optical disc.

The baryonic component of the RAR is typically constructed from the distribution of stars and H I gas. The conversion from light to mass is derived using stellar population synthesis models, and a fixed Υ_* value in the near-infrared wavelength range has been found to provide an effective dust-free tracer of the older stellar population. This is also less sensitive to variations in parameters like age and metallicity compared to the optical bands (Bell & de Jong 2001; Meidt et al. 2014; Norris et al. 2014; Röck et al. 2015). For example, many

studies use a constant mass-to-light ratio using the *Spitzer* 3.6 μm band, ranging from $\Upsilon_* = 0.42$ (Schombert & McGaugh 2014) to $\Upsilon_* = 0.6$ (Meidt et al. 2014). Lelli, McGaugh & Schombert 2016 adopted a value of 0.7 for the bulge and 0.5 for the disc component using Spitzer 3.6 μm photometry for the SPARC database.

However, one persistent source of uncertainty in constructing the baryonic component of the RAR is the assumption of a constant mass-to-light ratio, $\Upsilon_\star$. In this paper, we aim to address this in a homogeneous way with a sample of H I-selected galaxies that have excellent multiwavelength ancillary data from which we can measure accurate $\Upsilon_\star$ ratios with spatially resolved SED fitting and probe the low acceleration regime of the RAR. Combined with H I kinematics, these observations enable us to construct both the baryonic (stars and gas) and the dynamical components required to probe the RAR at low acceleration beyond the very local Universe.

This paper is organized as follows. In Section 2 we outline the MIGHTEE-HI data we use to form a sample of 19 galaxies with which to investigate the RAR. In Section 3 we describe the photometric measurements to determine the radial stellar-mass surface density and the mass-to-light ratios of our galaxies along with the measured rotation curves and the surface mass density of H I. In Section 4 we present our results and in Section 5 we discuss our results and summarize our conclusions. Throughout the paper we assume ΛCDM cosmology with $H_0 = 70$ kms^{-1} Mpc^{-1}, $\Omega_m = 0.3$, and $\Omega_\Lambda = 0.7$. Unless otherwise stated, all logarithms are base 10.

2 DATA

2.1 MIGHTEE-HI

The MeerKAT International GigaHertz Tiered Extragalactic Exploration survey (MIGHTEE; Jarvis et al. 2016), is a medium-deep, medium-wide survey providing simultaneous radio continuum (Heywood et al. 2022; Hale et al. 2025), spectral line (Heywood et al. 2024), and polarization observations (Taylor et al. 2024). MIGHTEE covers an area over 20 deg^2 over four well-known extragalactic deep fields: COSMOS, XMM-LSS, Extended Chandra Deep Field South (ECDFS), and ELAIS-S1.

The MIGHTEE-H I emission project represents one of the first deep, blind, medium-wide interferometric surveys for neutral hydrogen. The Early Science spectral line products are described in detail in Maddox et al. (2021). The MIGHTEE Early Science data has led to various publications and scientific results, including Ponomareva et al. (2021), which is particularly relevant to this paper. This study defined a sample of 67 galaxies from the MIGHTEE Early Science data to measure H I rotation curves, analyse their kinematics, and investigate the bTFR over the past billion years.

Building on these results, this work makes use of the first major data release (DR1) of the MIGHTEE-H i deep spectral line observations in the COSMOS field (Heywood et al. 2024), which provides eight times better spectral resolution compared to the Early Science data. The DR1 imaging products were created from 94.2 h of on-target observations using 15 pointings. The HI imaging products achieve an angular resolution of 12 arcmin at z = 0. The spectral line observations cover two interference-free regions, namely L1 ($0.23 < z_{HI} < 0.48$) and L2 ($0 < z_{HI} < 0.1$), of MeerKAT's *L*-band (856–1712 MHz) with a spectral resolution of 26 kHz (equivalent to 5.5 km s^{-1} at z = 0) for L2, and 104.5 kHz for L1. Both the L1 (960–1150 MHz) and L2 (1290–1520 MHz) sub-bands were also imaged with three different resolution settings. A detailed description of the DR1 data is available in (Heywood et al. 2024). The DR1 imaging products from MIGHTEE-H I, with the higher spectral resolution, lay the foundation for more accurate H I kinematics required for this paper.

2.2 Optical and near-infrared data

In this work, we leverage the wealth of deep multiwavelength data over the COSMOS field, which are crucial for stellar mass measurements to complement the H I observations. Optical *u*-band photometry is sourced from CFHT (Cuillandre et al. 2012), while *GRIZ* photometry is provided by the HyperSuprimeCam Subaru Strategic Program (HSC; Aihara et al. (2018, 2019)). For the near-infrared *YJHK$_s$* photometry, we rely on the UltraVISTA (McCracken et al. 2012) Data Release 6 imaging. The 5σ depth of these data are in the range 25–27 mag (AB) for a 2 arcsec aperture (see table 1 in Adams et al. 2023, for more information), thus they are significantly deeper than the data usually available for photometric measurements of relatively low-redshift galaxies. We note that a further advantage of using these data, is that the imaging all has approximately the same seeing (~ 0.8 arcsec), mitigating the need for significant aperture corrections between bands. This is also the reason that we do not use the *Spitzer* 3.6 μm band in this study, as the resolution is a factor of ~ 3 poorer than the ground-based optical and near-infrared data that we use.

2.3 Sample selection

Based on the MIGHTEE-DR1, we select all galaxies with inclinations greater than 20°, as measured from the H I moment-0 maps to ensure reliable kinematic measurements. We also require that they are extended across at least three resolution elements along their major axes in the MIGHTEE data. Further details of the selection and automated kinematic modelling can be found in Ponomareva et al. (2021).

This results in a sample of 19 galaxies to study the radial acceleration relation, focusing on those with high-quality, resolved rotation curves, up to $z = 0.08$ (Ponomareva et al., in preparation). This purely H I-selected data set, complemented by the detailed photometry across 10 optical and near-infrared bands described above, is thus ideal for exploring the radial acceleration relation from the perspective of a sample selected on the H I gas mass. Such H I selection predominantly results in a sample of low-mass disc galaxies with relatively low stellar mass, and as such enable us to probe predominantly the low-acceleration part of the RAR.

3 METHODS

3.1 Photometry

We extract resolved optical and near-infrared photometry of the low-redshift H I galaxies in the COSMOS field using the PHOTUTILS package (Bradley et al. 2024).

3.1.1 Isophotal fitting

Cutouts were created for all galaxy images, centring each on the target galaxy, followed by background subtraction. Source detection was performed using image segmentation via the PHOTUTILS detection tool, identifying all sources with at least 10 connected pixels above a 2σ threshold. To isolate the target galaxy, we applied two masking steps: a manual masking of foreground stars that overlap with the galaxy of interest if applicable, and an automatic masking of unrelated sources (galaxies, stars) in the image using the segmentation map. We then modified the segmentation map to

retain only the galaxy and background pixels, setting all other sources to zero, yielding an image free of flux contamination from nearby objects. Elliptical isophotes were then fitted to the surface brightness distribution of each galaxy using PHOTUTILS, following Jedrzejewski ([1987](#)). Accurate masking is crucial to ensure reliable photometric measurements and relatively straightforward for smooth, regular galaxies, however it can become problematic in late-type systems where clumps of star formation in the disc are hard to distinguish from foreground stars, for example. To mitigate these effects, we employed sigma clipping during the isophote fitting to exclude deviant points, improving the stability and accuracy of the fits in low surface brightness regions or in galaxies with prominent non-elliptical features such as spiral arms. The fitting process begins with an initial elliptical isophote, defined by estimated values for the centre (x, y), ellipticity, and position angle of the galaxy. The image is then sampled along this elliptical path to generate a 1D intensity profile as a function of angle, from which the mean intensity and pixel count within the isophote are measured. The algorithm proceeds by incrementally adjusting the semimajor axis, using the parameters of the previous fitted ellipse as the starting point for each subsequent fit. The isophotal analysis returns, for each fitted ellipse, the mean intensity along the elliptical path in surface brightness units, ellipticity, and position angle (PA), along with their associated uncertainties. The surface brightness profiles are then extracted from the mean intensity values, excluding masked regions.

It is important to point out that when fitting elliptical isophotes, the ellipticity and position angle of the isophotes can vary significantly with radius and across different photometric bands, due to different galaxy components. While this variability can be useful for detailed studies of galaxy structures like bars and spiral arms that leave distinct signatures in the radial surface brightness profile of galaxies, it can result in inconsistently sampling the same physical regions of a galaxy. This consistency is crucial for later deriving stellar masses and surface mass densities using SED fitting.

Since PHOTUTILS is optimized to fit elliptical isophotes, particularly in early-type galaxies, attempting to simultaneously fix all the isophote parameters caused the fitting algorithm to fail. To address this, we adopted an alternative method, that consisted of three main steps. First, we used the `fit image` task and allowed the ellipticity and position angle to vary freely, keeping only the centre fixed. We chose the HSC G band as a reference due to its depth, with a 5σ AB limiting magnitude of 27.4 mag (Aihara et al. [2022](#)). The G-band effectively captures key structural features and extends far enough into the outer disc of galaxies for a robust comparison of the H I and stellar disc morphologies. We also verified our results using the R-band, our second deepest band with a 5σ AB limiting magnitude of 27.1 mag, traditionally used to derive optical inclinations, as it is more sensitive to the older stellar population that traces stellar mass. The inferred axis ratios are consistent between G- and R-bands within uncertainties. Second, we used the outermost isophote from the G-band fit to define a fixed geometry – fixing the centre, ellipticity, and position angle–which was visually inspected to ensure it provided a good overall description of the galaxy morphology. Finally, based on this geometry, we extracted surface brightness profiles in all optical and near-infrared bands via the ELLIPSE SAMPLE method. This ensured consistent sampling of physical regions across bands and avoided the convergence issues associated with trying to fit all parameters at once. An example of using the method outlined above can be seen in Fig. [1](#) for a representative galaxy in our sample. We then computed the uncertainties in both position angle and axis ratio by summing in quadrature the PHOTUTILS error of the outermost isophote and the standard deviation from multiple measurements.
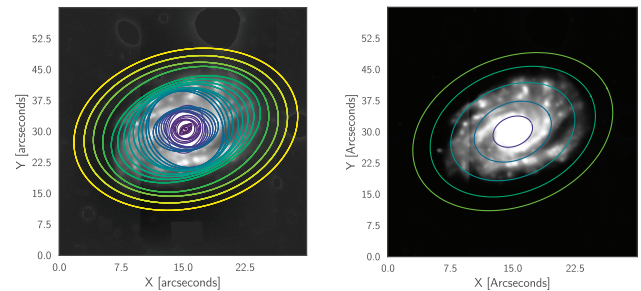

Figure 1. *Left*: Elliptical isophotes on the G-band image with varying position angle and ellipticity for one of our galaxies. *Right*: Elliptical apertures that we use for the analysis on the same image placed every 5 arcsec with fixed centre, position angle, and ellipticity.

3.1.2 Correcting for inclination

The inclinations of galaxies play a key role in this study, as they affect both the surface brightness profiles and the derivation of rotational velocities from H I kinematics. Typically, inclinations can be derived from both optical and H I data (Verheijen [2001](#)). In general, the H I disc is much thinner than the stellar disc and its intrinsic thickness can be neglected but due to flaring, it can become significantly thick in the outer parts (Bacchini et al. [2019](#); Mancera Piña et al. [2025](#)). Since our HI data is only marginally resolved, we choose to adopt the optical inclinations, as our optical data is sufficiently deep to reliably trace the underlying stellar disc. The inclinations (i) were derived from the axis ratio using the standard relation:

$$\cos^2(i) = \frac{(b/a)^2 - q_0^2}{1 - q_0^2}, \qquad (1)$$

where b and a are the semimajor and semiminor axes in G-band, and q_0 represents the intrinsic axis ratio of the disc, typically between 0 (thin disc) and 0.4 (Fouque et al. [1990](#)). In our analysis, we adopt the thin disc assumption with $q_0 = 0$. We verified that assuming different q_0 values (thin disc with $q_0 = 0$, or following standard prescriptions with $q_0 = 0.2$) had a negligible impact on the derived inclinations, with variations well within the uncertainties. The specific intensity (flux per unit area) varies with inclination, such that in highly inclined galaxies the surface brightness increases as the projected area of the galaxy is decreased from its face-on value. To obtain accurate measurements, it is therefore essential to correct for this projection effect by adjusting the observed surface brightness $(\mu_{\rm obs})$ to its face-on surface brightness value (μ_0) at each radius using:

$$\mu_0 = \mu_{\rm obs} - 2.5 \log_{10} b/a. \qquad (2)$$

We also applied Galactic extinction corrections using Schlegel dust extinction maps (Schlegel, Finkbeiner & Davis [1998](#)) that employ a $R_V = 3.1$ extinction curve, using the appropriate extinction coefficients corresponding to the different photometric bands. In the near-infrared, these were taken from the VISTA technical information. For the optical bands, however, we utilized the Python package EXTINCTION that is commonly used to calculate the Galactic extinction and reddening at a given wavelength based on the Fitzpatrick ([1999](#)) model, given a certain R_V. The average extinction in G and R bands is ≈ 0.07 mag and only 0.006 for the K_s-band. This reflects the benefits of using the data across the COSMOS field as it lies at high Galactic latitude and therefore suffers minimal galactic extinction. The surface brightness was measured for each galaxy over a range of elliptical isophotes and the total integrated flux in each photometric band was obtained by summing the pixel values within

the largest fitted elliptical isophote. To measure the uncertainties on the fluxes, circular apertures with areas equal to that of the fitted ellipse at a specific semimajor axis were randomly placed within a larger cutout image, ensuring they were placed outside other bright sources or galaxies. A Gaussian was fitted to the histogram of flux values measured in these apertures, and the standard deviation of the fitted Gaussian was used as an error estimate for the flux within the specified aperture. This method ensures that the calculated errors reflect the noise characteristic of the specific aperture size.

3.1.3 SED fitting

The total fluxes in all bands were used to measure the stellar masses through spectral energy distribution (SED) fitting for each galaxy. To achieve this, we employed the BAGPIPES code (Bayesian Analysis of Galaxies for Physical Inference and Parameter Estimation; Carnall et al. 2018). BAGPIPES contains several star formation history (SFH) models, including: exponential, delayed exponential, log-normal and double power law and uses a Chabrier Initial Mass Function (IMF; Chabrier 2003) with Stellar Population Synthesis models based on Bruzual & Charlot (2003), with three dust extinction models: Calzetti (Calzetti et al. 2000), Cardelli Milky Way dust law (Cardelli, Clayton & Mathis 1989) and (Charlot & Fall 2000). It works on the assumption of energy balance where the strength of dust emission is equal to the amount of energy removed from the UV-optical by the dust attenuation.

We tested several parametric star formation history models, however the choice of SFH did not affect the final stellar mass results. In fact, for most of the MIGHTEE-HI galaxies, no star formation history (SFH) model is preferred over the other (Tudorache et al. 2024). Therefore, for the rest of this analysis, we fit all our photometry with the delayed exponential model. We model the dust attenuation using the Calzetti law by allowing the extinction to vary between $A_V = 0 - 2$, whilst keeping the redshift fixed as all of our galaxies have precise redshifts from their HI emission line. We note that the choice of extinction law does not affect our results. We employ the stellar grids that contain remnants, i.e. the stellar mass included in white dwarfs, neutron stars, etc., but exclude gas lost by stellar winds or supernovae. For the rest of this paper, we quote stellar masses and surface mass densities including remnants, if not specified otherwise.[1]

We obtain the total stellar masses, $M_\star$ for all our galaxies using the photometry across the 10 photometric bands. Fig. 2 illustrates an example of an SED fit obtained for a galaxy in our sample. The uncertainties on the stellar masses are based on the posterior distributions from BAGPIPES and do not take into account systematic uncertainties that arise from the choice of IMF or star-formation history for example. The near-infrared photometry is particularly useful to robustly estimate the total stellar masses, as it is minimally affected by dust attenuation and recent star formation episodes. The total stellar masses for our samples can be found in Table 1.

3.1.4 Resolved stellar mass surface densities

After deriving the stellar masses, we compute the resolved stellar mass surface densities for the galaxies in our sample. To achieve this, we first fit their surface brightness profiles with an analytical

---

[1]We tested both scenarios, both with remnants and without, and it does not significantly impact our final results of stellar masses, stellar surface densities, or mass-to-light ratios.
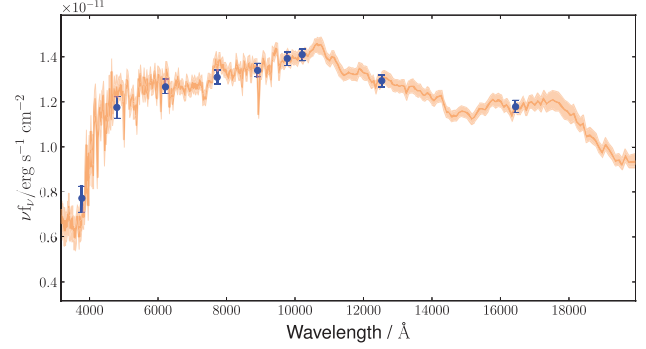
Figure 2. An example of SED fit with BAGPIPES across the 10 photometric bands, from HSC *ugrizy* and VISTA *YJHKs*. The input photometry is given by the blue points and the orange line is the posterior SED, both presented in the rest-frame.

Table 1. Redshifts, optical inclinations, stellar masses, and total mass-to-light ratios in K_s−band for the galaxies in our sample. Stellar masses are derived from SED fitting using a delayed exponential star formation history (Mobasher et al. 2015), with uncertainties reflecting the posterior distributions obtained from BAGPIPES.

Galaxy	z	$i_{\rm opt}$ (°)	$\log_{10}(M_\star/M_\odot)$	$\Upsilon_\star$ (M$_\odot$/L$_\odot$)
J095846.8+022051	0.00577	70	7.48 ± 0.08	0.33 ± 0.08
J095927.9+020025	0.01297	41	7.65 ± 0.10	0.35 ± 0.09
J100005.8+015440	0.00622	66	7.82 ± 0.06	0.53 ± 0.08
J095904.3+021516	0.02458	50	7.98 ± 0.08	0.36 ± 0.08
J100211.2+020118	0.02134	41	9.18 ± 0.09	0.38 ± 0.08
J100009.3+024247	0.03267	56	9.49 ± 0.09	0.37 ± 0.07
J100115.2+021823	0.02845	73	8.79 ± 0.09	0.32 ± 0.06
J095720.6+015507	0.03205	48	10.10 ± 0.07	0.36 ± 0.06
J100143.2+024109	0.04699	45	9.43 ± 0.09	0.34 ± 0.06
J100259.0+022035	0.04426	43	10.92 ± 0.10	0.37 ± 0.10
J100055.2+022344	0.04426	42	10.53 ± 0.08	0.57 ± 0.10
J095923.2+024137	0.04764	61	9.75 ± 0.10	0.37 ± 0.08
J100236.5+014836	0.04554	44	9.47 ± 0.12	0.24 ± 0.07
J100117.1+020337	0.06155	47	9.50 ± 0.09	0.34 ± 0.07
J100003.9+015253	0.06521	60	9.19 ± 0.09	0.30 ± 0.07
J095755.9+022608	0.07125	76	10.08 ± 0.10	0.39 ± 0.09
J100217.9+015124	0.06238	49	10.31 ± 0.12	0.29 ± 0.07
J100103.7+023053	0.07193	39	10.09 ± 0.10	0.30 ± 0.08
J095907.8+024213	0.07908	46	10.81 ± 0.07	0.38 ± 0.06

model and then use these fits to convert the surface brightness into stellar mass surface density as a function of radius, $\Sigma_*(r)$.

Typically, surface brightness profiles of galaxies are well characterized by a Sersic profile (Sersic 1968):

$$I(R) = I_e \exp\left\{ -b_n \left[\left(\frac{R}{R_e} \right)^{1/n} - 1 \right] \right\}, \qquad (3)$$

where I_e is the intensity at the half-light radius, R_e and b_n is a constant that depends on the Sersic index n, with n describing the light profile or how concentrated the light is (with brighter and more massive galaxies having larger n values Caon, Capaccioli & D'Onofrio 1993). The constant b_n can be approximated by $1.992n - 0.3271$ (e.g. Capaccioli 1989; Prugniel & Simien 1997). For some galaxies in our sample that lack distinct bulges or contain pseudo-bulges, we evaluate whether this single Sersic profile more accurately describes the galaxy compared to a double Sersic model, containing both bulge and disc components. The latter is described by the following
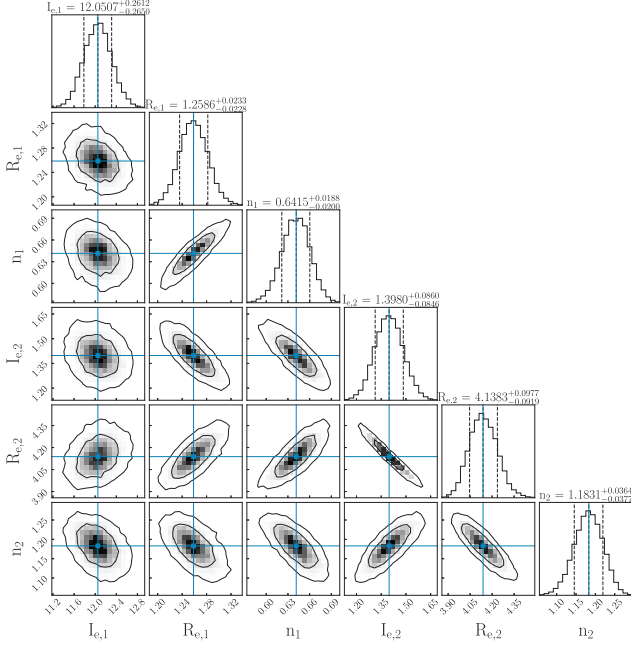
Figure 3. Example of posterior distribution for the set of six parameters describing the double Sersic function. The intensities at the half-light radius are given in units of μJy arcsec^{-2} and the radii are expressed in arcseconds. The blue lines represent the maximum likelihood estimates for the parameters, whilst the dashed lines show the 16th and 84th percentiles. Contours indicate the 68 per cent and 95 per cent confidence regions for the 2D posteriors.

functional form:

$$I = I_{e_1} \exp \left[-b_{n_1} \left(\frac{R}{R_{e_1}} \right)^{1/n_1} - 1 \right]$$
$$+ I_{e_2} \exp \left[-b_{n_2} \left(\frac{R}{R_{e_2}} \right)^{1/n_2} - 1 \right]. \tag{4}$$

To achieve this, we use NAUTILUS (Lange 2023), a nesting sampling algorithm that relies on Bayesian inference to estimate the best model and map the posterior distribution of the parameters, for the bulge I_{e_1}, R_{e_1}, n_1 and disc components I_{e_2}, R_{e_2} and n_2. We set uniform priors on the parameters of the Sersic function to cover the range in intensity and radius of our data points and set $0.5 < n < 4$. We use the Bayesian evidence (Z) to compare the single and double Sersic models, which represents the probability of the observed data given the model. Given two different models, the Bayes factor B is defined by:

$$\log_{10} B = \log_{10} Z(d|M_D) - \log_{10} Z(d|M_S), \tag{5}$$

where M_S and M_D are the double and single Sersic model that we are comparing. For all galaxies in our sample, the logarithm of the Bayes factor was > 9 indicating that the double Sersic model decisively fits the data better. We thus proceed to fit the surface brightness profiles with a double Sersic.

To recover the intrinsic, face-on surface brightness values, we convolve the model double Sersic profile with the PSF to match our data, and run NAUTILUS to derive the best fit values, as shown in Fig. 3. We fit this double Sersic model independently for each filter for every galaxy and calculate the surface brightness at fixed radii, employing a radial spacing of 0.6 arcsec. We use these surface brightness profiles in BAGPIPES to obtain the inclination corrected radial stellar mass surface densities. We visually inspect the SED fits
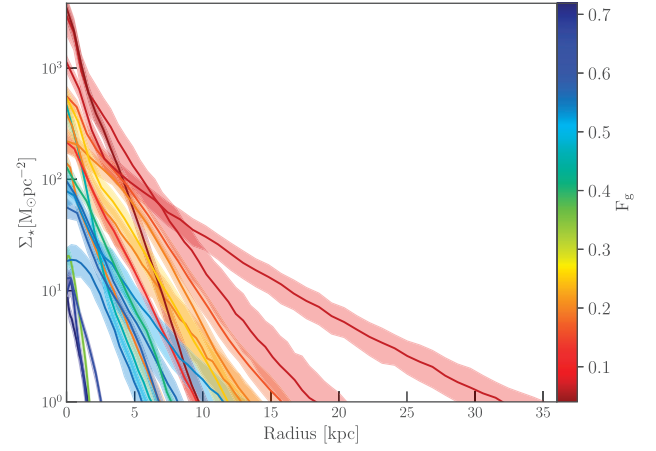
Figure 4. Resolved stellar surface mass densities for our sample of galaxies, colour coded by their gas fraction, $F_g = M_{HI}/M_{bar}$.

and the corner plots at every radius to ensure that the surface mass density Σ_* is robustly constrained. Fig. 4 presents all stellar mass surface densities obtained for our sample – high-mass galaxies have shallower declines in their surface brightness profiles, indicative of stellar contribution at all radii, whereas low-mass, gas-dominated galaxies show steeper declines.

3.1.5 Mass-to-light ratio variations

One of the most fundamental properties that can offer insights into the formation and evolution of a galaxy is its stellar mass, in addition to the luminosity produced by its stellar populations. The stellar mass-to-light ratio ($\Upsilon_\star$) enables a direct translation between photometry and dynamics. This plays a key role in rotation curve decomposition and mass modelling of disc galaxies, where it represents the major source of uncertainty and thus, the assumed mass-to-light ratio directly affects the inferred distribution of baryons and dark matter. Typically, the stellar mass-to-light ratio in different photometric bands is known to depend on stellar age, metallicity, IMF, and dust extinction and can be derived from stellar population models (Bell et al. 2003; Bruzual & Charlot 2003). Mass-to-light ratios are highly wavelength-dependent, especially in bluer filters, where there is substantial scatter. However, incorporating the near-infrared has been found to yield more robust stellar mass estimates, as the stellar mass-to-light ratios are less sensitive to age compared to UV or optical data (Into & Portinari 2013; Meidt et al. 2014; McGaugh & Schombert 2015). A constant stellar mass-to-light ratio has been commonly adopted in studies of galaxy dynamics to disentangle the contributions of dark matter and baryons to the total mass distribution. However, the systematic biases introduced by this assumption have only been quantified in a few studies, potentially affecting the accuracy of derived mass profiles and scaling relations (Ponomareva et al. 2018; Liang et al. 2025).

In this section, we aim to investigate mass-to-light ratio $\Upsilon_\star$ variations as a function of radius for all galaxies in our sample and compute the total $\Upsilon_\star$ for our galaxies. For this purpose, we use the near-infrared VISTA K_s-band, as near-infrared bands are less affected by dust and the light is emitted predominantly by the older stellar population that forms the bulk of the stellar mass (Sorce et al. 2013), as discussed previously. Additionally, at a wavelength of 2.2 μm, it is close to the commonly employed 3.6 μm band for similar studies (e.g. Verheijen 2001).

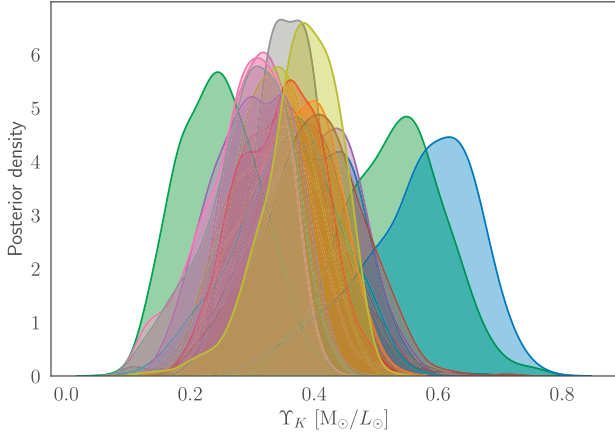**Figure 5.** Distribution of mass-to-light ratios in the K_s-band ($\Upsilon_\star$) from the mass-to-light ratio posterior samples derived from SED fitting with BAGPIPES.
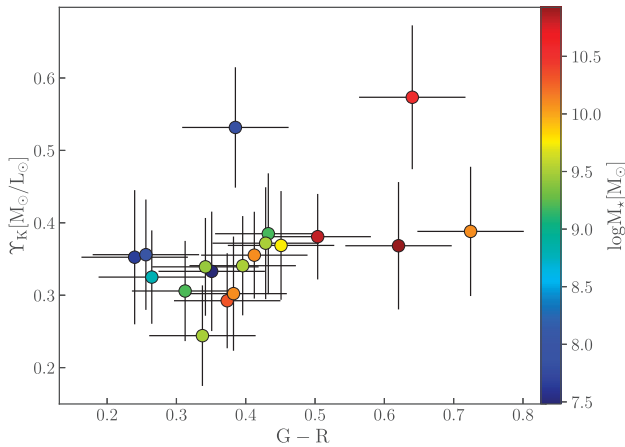

Figure 6. Mass-to-light ratio in K_s-band for our galaxies as a function of $G - R$ colour, colour coded by stellar mass.

The distribution of mass-to-light ratio in the K_s-band for our galaxies is shown in Fig. 5. We find that the total mass-to-light ratios obtained from SED fitting cover a wide range of values from 0.24 to 0.57, with a median of 0.35. These findings align well with those of Ponomareva et al. (2018), who employed a similar methodology, as well as with results from the DiskMass Survey (Martinsson et al. 2013). However, these values are in tension with recent studies such as Marasco et al. (2025), who used 2MASS K_s-band data and found a median $\Upsilon_\star = 0.7$, with significantly higher scatter. This discrepancy is likely due to their sample being a subsample of the more heterogeneous SPARC sample, which has a significantly larger fraction of high-stellar-mass galaxies that tend to exhibit higher mass-to-light ratios.

In Fig. 6 we show the mass-to-light ratio in relation to the $G - R$ colour. This shows a clear correlation, with a Pearson coefficient of 0.66. This trend is particularly relevant for our sample of late-type galaxies: lower $G - R$ values correspond to bluer, star-forming, disc-dominated systems that exhibit lower mass-to-light ratios, whereas redder $G - R$ values are associated with more bulge-dominated spirals and higher mass-to-light ratios.

To determine the radially-varying mass-to-light ratios, we use the ratio of stellar surface mass density, obtained from SED fitting, to the
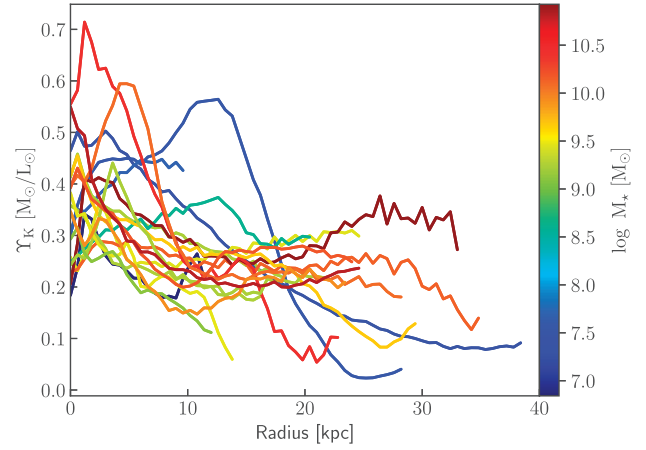
Figure 7. Mass-to-light ratio variations in K_s-band as a function of radius for all galaxies in our sample, colour coded by stellar mass. Unsurprisingly, the mass-to-light ratios are typically higher in the centre, followed by a decrease and flattening at large radii, where the surface brightness exponentially decreases.

K_s-band surface brightness, both inclination corrected and derived from the double Sersic profiles.

In Fig. 7 we show the radial variations in the mass-to-light ratio for all galaxies in our sample, colour-coded by stellar mass. The figure reveals a clear trend where the mass-to-light ratio is higher in the central regions and flattens beyond a certain radius.

These variations of Υ_* in the K_s band both as a function of radius and colour, suggest that a constant Υ_* is not appropriate to describe the complicated physics of disc galaxies when converting light to stellar mass.

3.2 H I surface density profiles and rotation curves

After deriving the stellar contribution, we must now compute the gas surface mass densities to assess their contribution to the baryonic component of the RAR.

Due to the faintness of the H I line, resolved observations of galaxies in H I become increasingly challenging at higher redshifts. Kinematic modelling requires H I observations with high spatial and velocity resolution, combined with a high signal-to-noise ratio (SNR), to accurately derive rotation curves. However, the new generation of large-scale H I surveys are transforming this landscape, coupled with new software developments that enable kinematic modelling even for marginally resolved galaxies.

These include ^{3D}Barolo (Di Teodoro & Fraternali 2015) and TIRIFIC (Józsa et al. 2012), that can effectively determine the underlying kinematics in galaxies with as few as three resolution elements along the major axis, provided that the signal-to-noise ratio (SNR) is greater than 2–3 (Di Teodoro & Fraternali 2015; Mancera Piña et al. 2020).

In this work, we use the software ^{3D}Barolo (3D Based analysis of Rotating Objects from Line Observations; Di Teodoro & Fraternali 2015), to derive rotation curves and radial H I surface density profiles. ^{3D}Barolo automatically fits a 3D tilted-ring model to emission-line data cubes. We use the 3D fit task that works with a masked data cube to exclude noisy pixels. The source mask is generated using MASK=SMOOTH with a signal-to-noise ratio threshold of 3 (SNRCUT=3). Additionally, we set NORM=AZIM for an azimuthal normalization of the moment-0 map to obtain the average gas surface
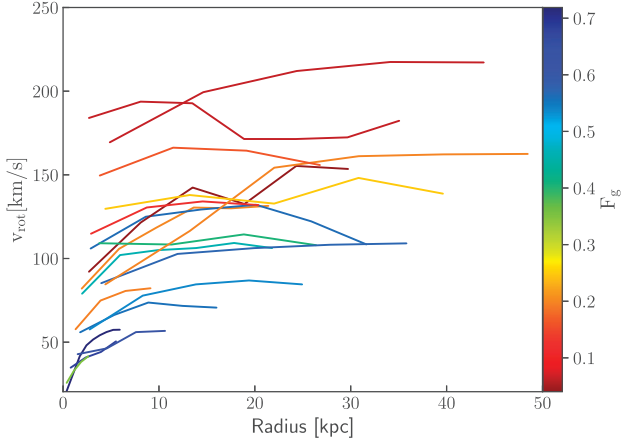
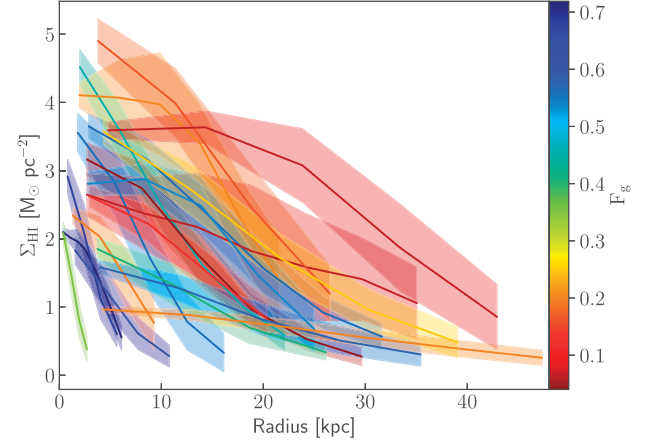**Figure 8.** Rotation curves for our sample of galaxies, colour coded by their gas fraction, $F_g = M_{HI}/M_{bar}$.

Figure 9. All HI radial surface densities derived using 3D BAROLO, colour coded by their gas fraction, $F_g = M_{HI}/M_{bar}$.

density Σ_{gas} for each ring in the model. Throughout the analysis, we assume a razor-thin H I disc. To account for beam smearing, ^{3D}Barolo convolves the model with the beam. The software also includes a built-in source finding algorithm that finds a galaxy in the cube and reliably estimates the galaxy's centre and systemic velocity during the initial run.

Despite this however, ^{3D}Barolo is sensitive to initial parameter guesses, particularly the inclination angle, which is more challenging to constrain in lower resolution data (see also fig. 2 in Ponomareva et al. 2021). Therefore, we input the inclination based on optical photometry, as discussed in Section 3.1.2, allowing it to vary within its uncertainties, while keeping other parameters free.

The fitting process consists of two steps: an initial fitting, where the rotation velocity, velocity dispersion, inclination, and position angle are all free parameters to fit, and a second step, where only the rotation velocity and velocity dispersion are fitted, while the inclination and position angle of the rings are fixed. We assume a radial separation equal to half the beam size, i.e. two rotation curve points per beam. The uncertainties on the rotation velocities are estimated using ^{3D}Barolo's default Monte Carlo error calculation method, implemented through the built-in function FLAGERRORS.

The rotation curves for our sample are presented in Fig. 8 (see also Ponomareva et al., in preparation).

After obtaining the rotation velocities, we also derive the azimuthally averaged H I surface mass densities at each radius, corrected for inclination. This allows us to quantify the baryonic contribution of the gas component to the total radial acceleration. The mean H I flux density is obtained at each radius from the input data cubes, corrected to face-on values, and automatically converted to physical units of $M_\odot \, pc^{-2}$ (Meyer et al. 2017) in 3D BAROLO. In disc galaxies, the dominant baryonic mass components are stars and atomic gas, and the contribution from molecular gas is typically small (Catinella et al. 2018). However, we should still account for these components insofar as it is feasible. We therefore apply a correction factor to the face-on H I surface densities to account for contributions from helium, metals, and molecular gas. The total gas mass, corrected for the hydrogen fraction (McGaugh et al. 2020), can be expressed as:

$$M_g = X^{-1}(M_{HI} + M_{H_2}), \qquad (6)$$

where M_{HI} and M_{H_2} represent atomic and molecular hydrogen, respectively. The total hydrogen fraction X is related is then related

to the stellar mass by

$$X(M_\star) = 0.75 - 38.2 \left(\frac{M_\star}{1.5 \times 10^{24} \, M_\odot} \right)^{0.22}. \qquad (7)$$

As we do not have a direct measurement of molecular gas for our sample of galaxies, we also use the stellar mass–molecular gas relation found by McGaugh et al. (2020), who have shown that the molecular gas mass is approximately 7 per cent of the stellar mass of a galaxy. In their work, they combined two known scaling relations between the molecular gas mass and star formation rate [see equation (1) in McGaugh & Schombert 2015] and between the stellar mass and star formation rate (McGaugh, Schombert & Lelli 2017), such that the molecular gas mass is given by:

$$\log_{10}(M_{H_2}) = \log_{10}(M_\star) - 1.16. \qquad (8)$$

The molecular gas mainly contributes to the baryonic radial acceleration in the central regions of galaxies (Young & Scoville 1991; Leroy et al. 2008; Saintonge et al. 2016; Saintonge & Catinella 2022). As a result, not including it in the baryonic budget can lead to an underestimation of g_{bar} in the inner regions (higher acceleration).

We apply these correction factors to the face-on H I surface densities, which are presented in Fig. 9, to determine the total gas surface density as a function of galaxy radius.

3.3 Baryonic circular velocities

We use the stellar and gas surface mass density profiles and numerically solve Poisson's equation to compute the circular velocity contribution of each baryonic component to the total rotation curves, where the total baryonic circular velocity is given by the sum in quadrature of the individual contributions from the gas and stars.

We use the GALPYNAMICS software (Iorio 2018), which numerically solves Poisson's equation under the assumption of vertical hydrostatic equilibrium (Cuddeford 1993). The software takes as input the mass surface density profiles and returns the circular velocity at each radius.

For the stellar component, we use the surface mass densities derived from SED fitting and model them with a fourth-degree poly-exponential function, following Bacchini et al. 2019 and Mancera Piña et al. 2022:

$$\Sigma_\star(R) = \Sigma_0 \exp\left(-\frac{R}{R_d}\right)(c_1 R + c_2 R^2 + c_3 R^3 + c_4 R^4), \qquad (9)$$
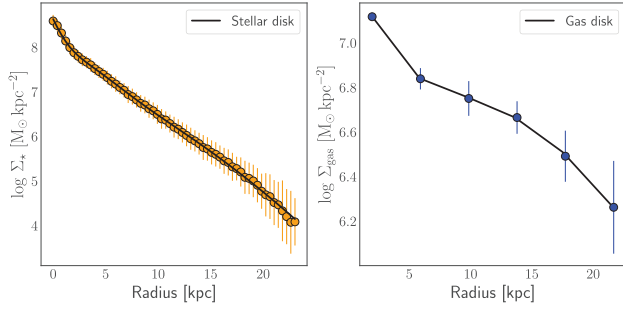
Figure 10. Radial stellar and gas surface density profiles for a representative high mass galaxy. The observed data points are shown alongside the solid lines, which represent poly-exponential fits derived using GALPYNAMICS. Error bars smaller than the size of the markers are not displayed.
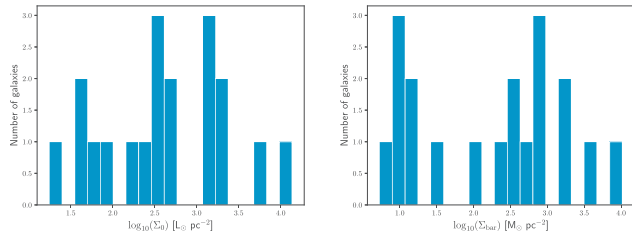

Figure 11. The central surface brightness Σ_0 and equivalent surface density distribution ($\Sigma_{\rm bar} = \frac{3}{4}\frac{M_{\rm bar}}{R_{\rm bar}^2}$, where $M_{\rm bar}$ is the baryonic mass (stars and gas), and $R_{\rm bar}$ is the radius where the baryonic circular velocity $v_{\rm bar}$ is maximum) histograms for our sample of 19 H I galaxies.

where Σ_0 is the central surface mass density, R_d is the disc scale length, and c_1, c_2, c_3, c_4 are the coefficients of the polynomial. This functional form is flexible enough to capture the rich structure of stellar profiles, including any dips and peaks, and any deviations from a simple exponential. In addition to the radial distribution, the vertical mass distribution of the stellar disc must also be specified. Several functional forms have been used in the literature, such as sech^2, sech, and exponential profiles (van der Kruit 1988; Bershady et al. 2010). We test both a sech^2 and an exponential vertical profile. The sech^2 profile, often used in galactic disc models, arises from the assumption of isothermal vertical equilibrium and has a scale height h_z related to the disc scale length by $h_z = 0.1 R_d$ (van der Kruit & Freeman 2011). For the exponential case, we adopt a constant scale thickness of $z_d = 0.196\, R_d^{0.633}$, following the empirical relation from Bershady et al. (2010) based on photometry of edge-on galaxies. We find that the choice of vertical stellar distribution has a minimal impact on the resulting RAR. Therefore, for simplicity, we adopt an exponential stellar vertical profile with a fixed scale height in all subsequent analysis and present our results based on this configuration.

For the gas component, we assume a razor-thin disc in the modelling. This assumption is justified given that all galaxies in our sample are marginally resolved in H I, and that, in the mass regime of our galaxies, differences between thin and realistic flared gas discs have a negligible effect on the gravitational potential (see Mancera Piña et al. 2022). The radial surface-density profiles are modelled either with a simple exponential or, for more complex cases, a third-order poly-exponential function. These functional forms for both stars and gas, effectively model the variety of observed radial surface mass density profiles of the galaxies in our sample. An example of
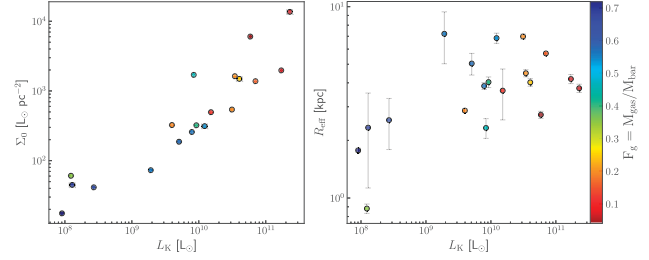
Figure 12. Luminosity in K band versus central surface brightness (left) and effective radius (right) for our sample of galaxies. Error bars smaller than the size of the markers are not displayed.
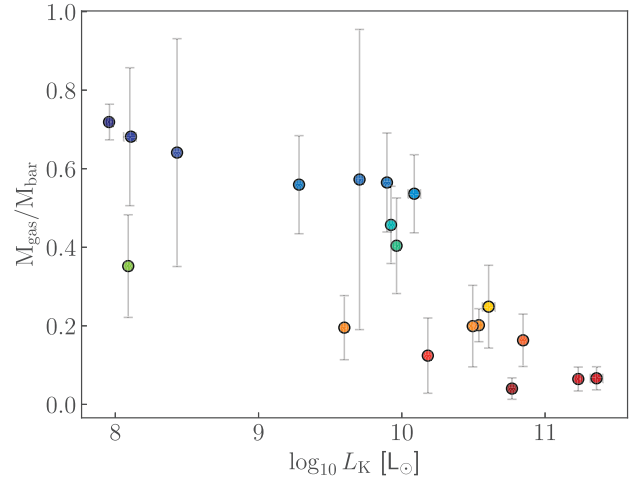

Figure 13. The gas fraction $F_g = M_{\rm gas}/M_{\rm bar}$, as a function of total K-band luminosity for our sample of galaxies. The gas fraction anticorrelates with L_K. Error bars smaller than the size of the markers are not displayed.

poly-exponential fits to the surface density profiles of stars and gas is shown in Fig. 10 for a representative galaxy in our sample.

To estimate the uncertainties on the circular velocities, we resample the radial stellar and gas surface densities used in GALPYNAMICS based on their associated errors. Assuming a Gaussian error distribution, we generate 100 realizations of the stellar and gas disc models by drawing new values for the surface densities ($\Sigma_\star$, Σ_{gas}) and scale lengths (R_d) from distributions centred on their best-fitting values with standard deviations set by their respective uncertainties. For each realization, GALPYNAMICS numerically solves for the circular velocity of the stellar and gas components. The final uncertainties on the star and gas circular velocities are then derived from the standard deviation of the resulting velocity distributions for all resampled models. Note that we do not correct for pressure support as this is negligible for the high rotational velocities of our sample (Iorio et al. 2017; Mancera Piña et al. 2021). As such, the rotation velocity of the gas is a direct tracer of the gravitational potential.

The overall properties of our galaxies are shown in the histograms in Fig. 11. Figs 12 and 13 show the central surface brightness, effective radius, and gas fraction as a function of total K band luminosity for our sample.

4 RESULTS

The contributions from stars and gas are added together, and the derivative of the potential gives the required baryonic acceleration:

$$g_{\mathrm{bar}}(r) = -\frac{\partial \Phi}{\partial r} = \frac{v_{\mathrm{bar}}^2(r)}{r}, \tag{10}$$

where g_{bar} is the acceleration due to the baryonic mass, v_{bar} is the circular velocity resulting from the baryonic mass, both determined at radius r.

The total centripetal acceleration, derived from rotation curves, is given by:

$$g_{\mathrm{obs}}(r) = \frac{v_{\mathrm{rot}}^2(r)}{r}, \tag{11}$$

where $v_{\mathrm{rot}}(r)$ is the velocity measured from the rotation curve at radius r.

The baryonic and dynamical acceleration components allow us to analyse the radial acceleration relation at all radii. Due to the angular resolution of our H I data, we discard the innermost points, which correspond to less than 5 arcsec in radius. The radial acceleration relation for our sample, derived using the varying mass-to-light ratio, is shown in Fig. 14, colour coded by the equivalent baryonic surface density. This quantity was introduced by McGaugh (2005) and is given by $\Sigma_{\mathrm{bar}} = \frac{3}{4} \frac{M_{\mathrm{bar}}}{R_{\mathrm{bar}}^2}$, where M_{bar} is the baryonic mass (stars and gas), and R_{bar} is the radius where the baryonic circular velocity v_{bar} is maximum.

4.1 Fitting the RAR

We model the RAR using two functional forms: the MOND-inspired relation from McGaugh et al. (2016) ('RAR' or 'McGaugh–Lelli– Schombert' interpolating function) and a general double power law proposed by Lelli et al. (2017). These were both fit using the Python package ROXY (Bartlett & Desmond 2023). This implements the 'Marginalized Normal Regression (MNR)' method, which fits a function to data accounting for uncertainties in both x and y, intrinsic scatter in the relation and unknown 'true' x values through the use of a Gaussian hyperprior with inferred mean μ_{gauss} and standard deviation w_{gauss}. We apply MNR to the accelerations in base 10 logarithmic space, so that both μ_{gauss} and w_{gauss} are expressed in dex. Extensive mock tests showed that MNR, unlike most others methods employed in the literature, is unbiased (Bartlett & Desmond 2023). The likelihood is sampled using the No U-Turn Sampler (NUTS) method of Hamiltonian Monte Carlo.

The MOND-inspired functional form (McGaugh et al. 2016) is described by the following equation:

$$g_{\mathrm{obs}} = F(g_{\mathrm{bar}}) = \frac{g_{\mathrm{bar}}}{1 - e^{-\sqrt{g_{\mathrm{bar}}/a_0}}}, \tag{12}$$

where a_0 represents the acceleration scale.

We adopted uniform priors for $\log_{10}(a_0)$ between -15 and 5, and for the intrinsic scatter between 0 and 3 dex. Running ROXY with 700 warm-up steps and 5000 samples (ample to ensure convergence), we recovered a best-fitting value of the acceleration scale $a_0 = (1.69 \pm 0.13) \times 10^{-10}$ ms^{-2} and an intrinsic scatter of 0.045 ± 0.022 dex. This is significantly smaller than the 0.12 dex total scatter reported by Lelli et al. (2017) for SPARC galaxies, and consistent with more recent estimates of the intrinsic scatter (Li et al. 2018; Chae et al. 2021, 2022; Desmond 2023), although we note the small dynamic range in g_{bar} for our sample.

To overcome some of the problems associated with the relatively small dynamic range, we also perform a joint fit using our sample combined with the SPARC RAR data at high accelerations (above our highest value for $\log_{10} g_{\mathrm{bar}}$) for which we impose a quality cut to include only galaxies with inclinations greater than 30 degrees. The high-acceleration SPARC data are less likely to have a significant departure from their assumed mass-to-light ratio of 0.5 at 3.6 μm, as the high-acceleration points are largely derived from the inner parts of galaxies where the stellar populations are generally older and more homogeneous compared to the star-forming discs that dominate the low-acceleration part of the RAR. Running ROXY on this combined data set yields a best-fitting acceleration scale of $a_0 = (1.32 \pm 0.13) \times 10^{-10}$ ms^{-2} and an intrinsic scatter of 0.064 ± 0.007 dex. This decrease in a_0 is expected, as the combined sample spans a wider range of baryonic accelerations than our data set alone. In particular, the SPARC galaxies extend further into the high-acceleration regime, where the RAR follows the 1:1 line. By contrast, our galaxies are limited to $g_{\mathrm{bar}} \lesssim 10^{-10}$ ms^{-2} at the high acceleration end, primarily populating the lower acceleration regions, where the data points begin to peel away from the 1 to 1 line. The primary reason for this is our selection bias toward low-mass, gas-rich galaxies.

In Fig. 14 we present the posterior predictive RAR relations with 1, 2, and 3σ confidence intervals from our fitted model, shown as red shaded regions around the best-fitting relation. For comparison, we also overlay the best-fitting RAR from the combined data set in blue with the full posterior predictive. Notably, the combined best-fitting line does not align with the centre of the posterior of the fit to our data alone, but instead lies outside the 2σ confidence region. This suggests that our data alone favours a different acceleration scale than the combined sample, which is dominated by the high-mass SPARC galaxies.

The deviation of our data set from the combined best-fitting RAR trend could stem from selection biases, as our sample is dominated by low-mass, gas-rich galaxies with lower baryonic accelerations. Furthermore, differences in the assumed mass-to-light ratios used to derive g_{bar} are likely to also play a significant role at these low accelerations, where the mass-to-light ratios in the outer regions of galaxies tend to be lower than in the central regions (Fig. 7). However, the very low intrinsic scatter in our RAR supports the conclusions of Lelli et al. (2017); Desmond (2023); Stiskalek & Desmond (2023), that the RAR is a fundamental relation.

The alternative functional form for the RAR: a general double power-law model, as proposed by Lelli et al. (2017), is given by:

$$y = \hat{y} \left(1 + \frac{x}{\hat{x}}\right)^{(\alpha - \beta)} \left(\frac{x}{\hat{x}}\right)^{\beta}, \tag{13}$$

where α and β are the high and low acceleration slopes for $x \gg \hat{x}$ and for $x \ll \hat{x}$, respectively. In the case of our data set alone, the limited sample size results in poor constraints on several parameters, particularly the high-acceleration slope α and $\log \hat{x}$.

To quantitatively assess the quality of both models, we computed the Bayesian Information Criterion (BIC):

$$\mathrm{BIC} = -2 \ln \hat{L} + k \ln(n), \tag{14}$$

where $\ln \hat{L}$ is the log-likelihood of the best-fitting model, k is the number of free parameters, and n is the number of data points. For our sample, the MOND-inspired fit is clearly favoured with a $\Delta \mathrm{BIC} = 10.6$, owing to its simpler form and fewer parameters to fit (1 compared to 4).

However, when we repeat the analysis on the combined data set (our sample + the high acceleration SPARC galaxies), the situation changes: the larger dynamic range in accelerations probed and improved statistics enable better parameter constraints, and the double power-law fit is preferred over the MOND-inspired model, with a
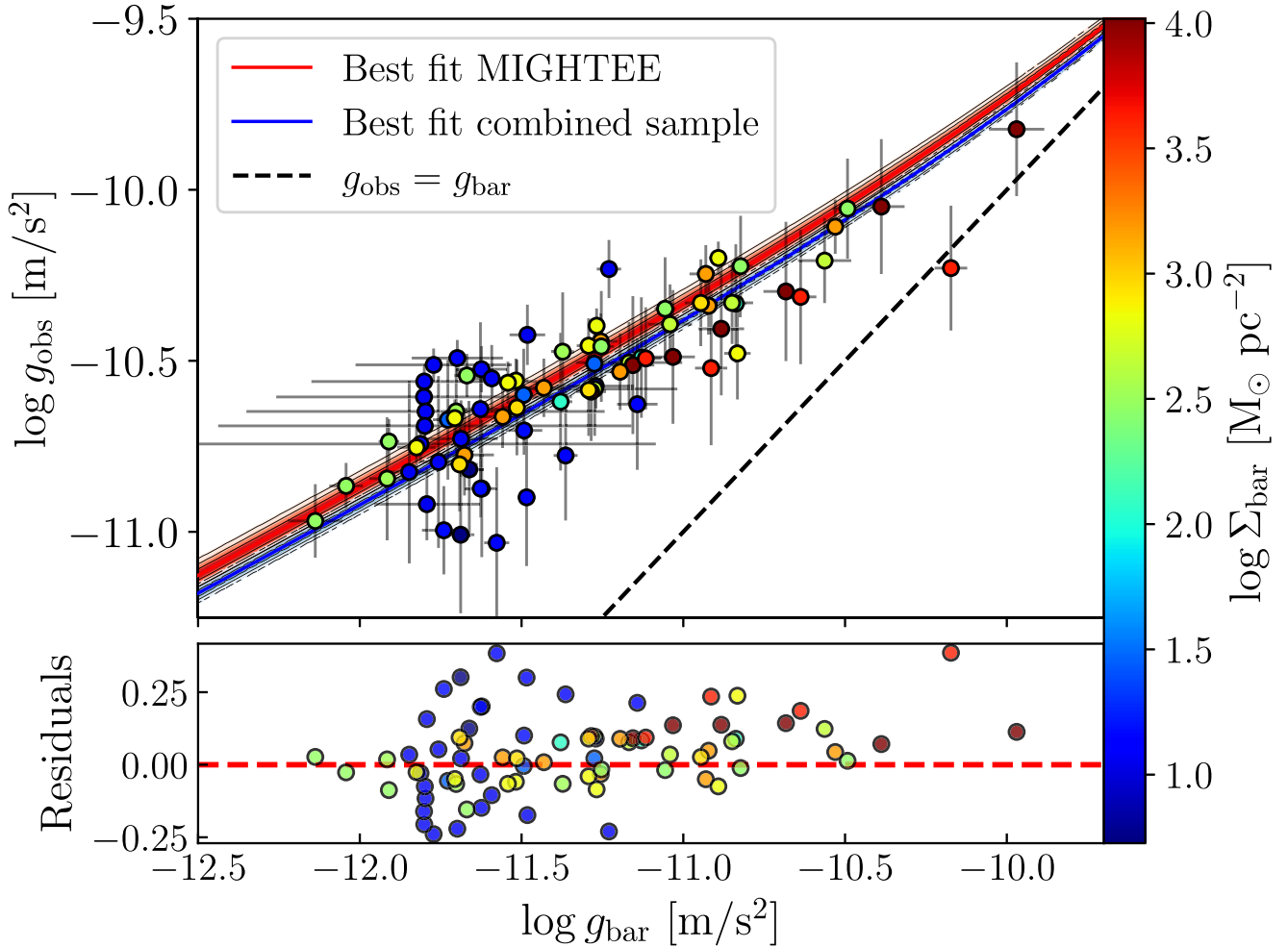
Figure 14. *Top*: The RAR for our sample of 19 late type galaxies, colour coded by their equivalent baryonic surface density. The red shaded regions represent the full posterior predictive distribution from the MOND inspired fit to our sample alone, shown at 1, 2, and 3σ confidence intervals, with the solid red line shown as the best fit. Similarly, the blue shaded regions and blue solid line represent the full posterior predictive distribution and best fit for the combined data set (our sample + high acceleration portion of the SPARC sample), not shown here. *Bottom*: The residuals (model − data) around the best-fitting model to our sample alone.

ΔBIC = 11.5. This suggest that the more flexible double power-law form better accommodates the full diversity of baryonic accelerations. The posterior predictive RAR relation for this case is shown in Fig. 15, and the best-fitting parameters are displayed in Table 2.

4.2 Effect of the mass-to-light ratio

As noted previously, past studies of the RAR have adopted a single mass-to-light ratio for galaxies spanning a range in mass and morphologies. In this section we therefore examine the impact of assuming a single, constant mass-to-light ratio for our sample, as well as a constant ratio for each individual galaxy within our sample (not including SPARC data in both cases). For the latter case, we adopt the average radial K_s-band mass-to-light ratio from the resolved SED fits. We perform the same fits to the RAR using equation (12) for these two cases and provide the results in Table 3. The RARs obtained based on these different $\Upsilon_\star$ assumptions are presented in Fig. 16.

In both cases, we recover an overall trend similar to that of the scenario of radially varying mass-to-light ratios. For the more massive galaxies where the average mass-to-light ratio approaches the standard value of 0.6 in the K_s-band (equivalent to ≈ 0.5 at 3.6 μm) in the central regions, this assumption has little effect, and the data points remain largely unchanged. However, at larger

radii (low g_{bar}), the points shift to higher accelerations. Under this simplification, the intrinsic scatter increases by 0.01 dex and the acceleration scale changes considerably from 1.69 to 1.08, deviating by nearly 4σ from our best-fitting a_0 obtained in the radially varying scenario.

Assuming a constant Υ_K across galaxy radii but allowing it to vary between galaxies has a comparable impact on the RAR. This similarity arises because the average integrated mass-to-light ratio for our sample is 0.36. For high-mass galaxies, an increase in Υ_K has a minimal effect at low accelerations, as the data points shift rightward but remain aligned with the overall trend. In the inner regions, assuming a constant Υ_K does not significantly change the results since the assumed value is already close to the true Υ_K in the centre. For lower mass galaxies, while the data points similarly shift to the right, the general RAR trend is still preserved, but the intrinsic scatter increases to 0.09 ± 0.02 dex.

In addition, we find that assumptions about the molecular gas content also have a non-negligible impact on the inferred RAR parameters. When molecular gas corrections are omitted, the intrinsic scatter does not decrease significantly ($\sigma_{int} = 0.038 \pm 0.021$ dex); however, the best-fitting acceleration scale changes by nearly 2σ to a value of $a_0 = 2.06 \pm 0.15$ m s^{-2} from the value obtained when molecular gas is included.
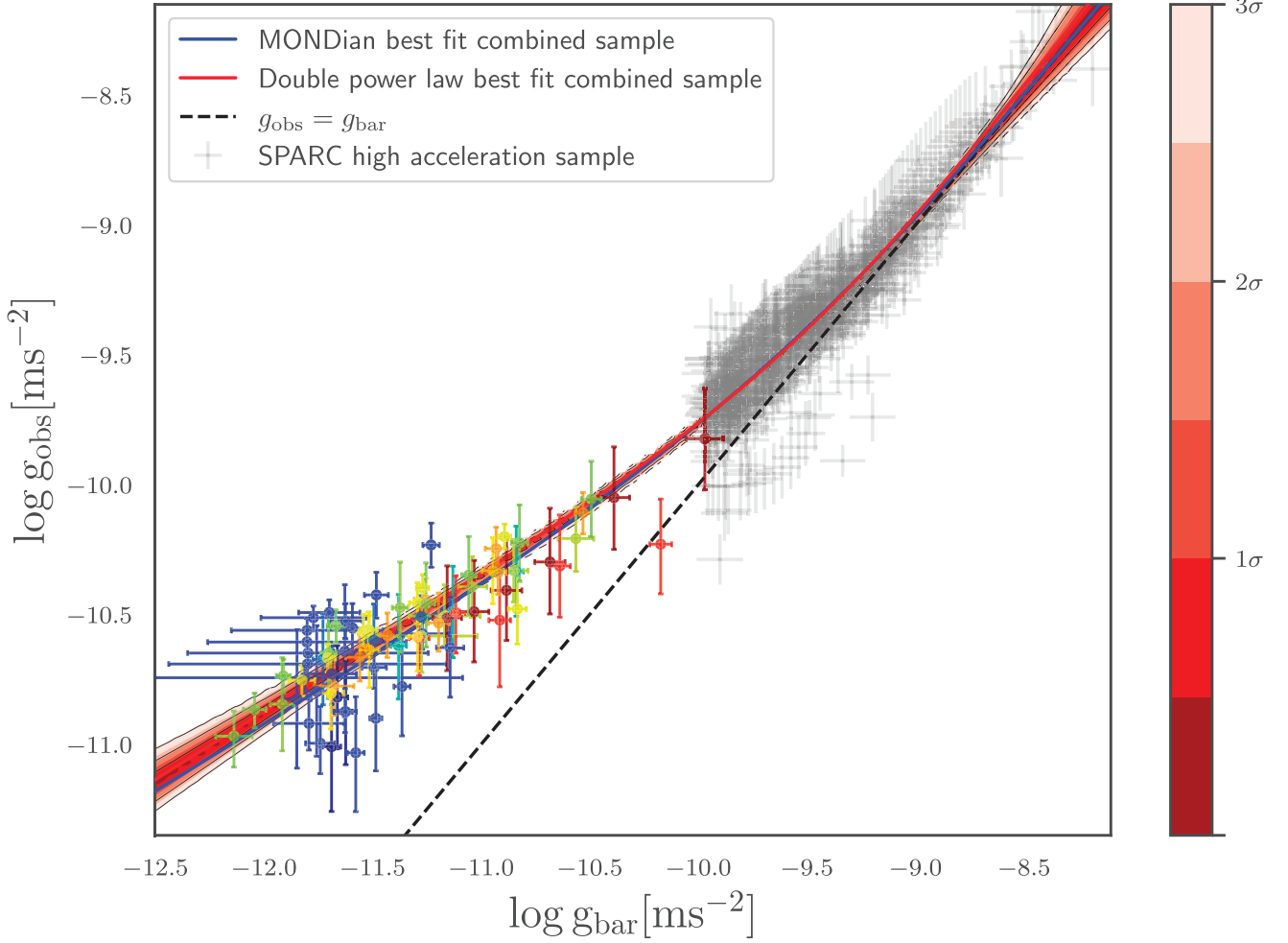
Figure 15. The posterior predictive plot for the combined sample (this work colour-coded by equivalent baryonic surface density + SPARC data in faded grey) at 1, 2, and 3 σ confidence intervals from the double power-law fit, with the MONDian best-fitting line in blue. Note that only the SPARC points with greater $g_{\rm bar}$ than our entire sample are included in our combined sample and shown here.

Table 2. Best-fitting parameters for the double power-law functional form of the RAR, derived using ROXY and including the combined sample (with SPARC high acceleration data points).

	$\hat{x}$ (10^{-10} m s^{-2})	$\hat{y}$ (10^{-10} m s^{-2})	α	β	$\sigma_{\rm int}$ (dex)	Sample size
This work	15.6 ± 18.5	4.5 ± 2.8	2.13 ± 1.42	0.46 ± 0.04	0.046 ± 0.022	80
Combined sample	3.5 ± 2.3	2.9 ± 1.3	1.10 ± 0.16	0.52 ± 0.03	0.062 ± 0.007	670

Table 3. Best-fitting acceleration scale (a_0) and intrinsic scatter ($\sigma_{\rm int}$) of the RAR under different $\Upsilon_\star$ assumptions, obtained using ROXY.

Sample	Fixed $\delta = 1$		Varying δ		
	a_0 (10^{-10} m s^{-2})	$\sigma_{\rm int}$ (dex)	a_0 (10^{-10} m s^{-2})	δ	$\sigma_{\rm int}$ (dex)
Varying $\Upsilon_K^{\rm fiducial}$	1.69 ± 0.13	0.045 ± 0.022	2.00 ± 0.15	3.94 ± 1.4	0.043 ± 0.021
Varying $\Upsilon_K^{\rm no\ mol}$	2.06 ± 0.15	0.038 ± 0.021	2.38 ± 0.17	3.69 ± 1.27	0.037 ± 0.021
Fixed $\Upsilon_K = 0.6$	1.08 ± 0.09	0.06 ± 0.02	1.48 ± 0.10	4.85 ± 1.21	0.032 ± 0.020
Radial average Υ_K	1.47 ± 0.13	0.09 ± 0.02	1.91 ± 0.15	4.22 ± 1.23	0.068 ± 0.020
SPARC RAR	1.15 ± 0.02	0.082 ± 0.003	0.96 ± 0.05	0.84 ± 0.03	0.081 ± 0.003
Low acceleration SPARC	1.16 ± 0.02	0.087 ± 0.003	0.85 ± 0.06	0.75 ± 0.03	0.084 ± 0.003
MIGHTEE + high acceleration SPARC	1.32 ± 0.13	0.064 ± 0.007	1.76 ± 0.15	1.29 ± 0.11	0.061 ± 0.007
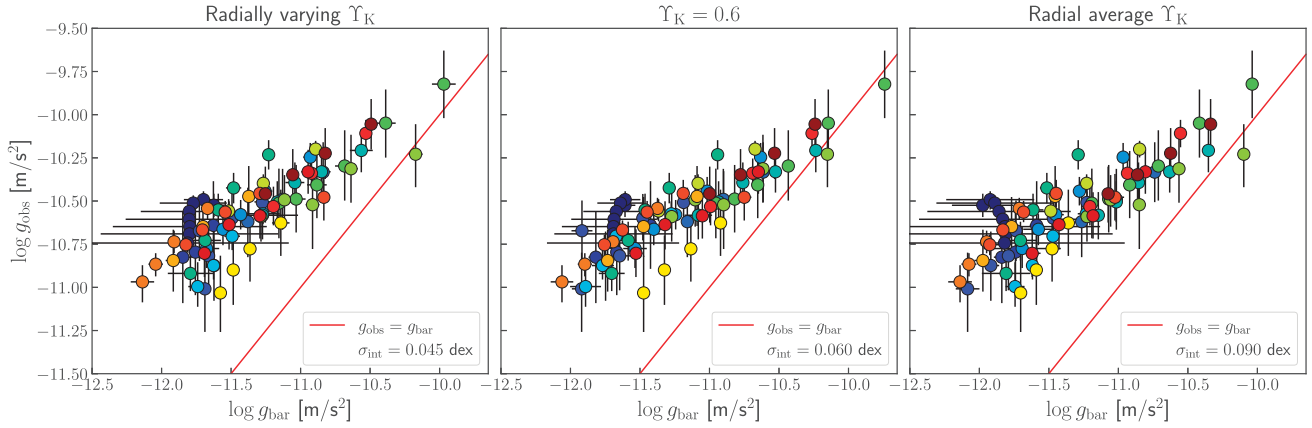
Figure 16. From left to right: the RAR obtained based on different assumptions of the mass-to-light ratio. First panel corresponds to the varying mass-to-light ratio case, the second to a constant $\Upsilon_\star$ ratio across galaxies and all radii and the third one to a different Υ_K between galaxies from the average value obtained from the resolved SEDs (see Appendix A for the resolved SEDs across galaxies' radii).

These results demonstrate that adopting a more sophisticated approach outperforms simpler assumptions, as it leads to significantly lower intrinsic scatter in the RAR. This underscores the importance of accounting for radial variations in mass-to-light ratios and the contribution from all components in the baryonic surface mass budget, particularly at the low-acceleration end, where such effects are most pronounced and predictions from MOND and ΛCDM are likely to be the most divergent. Neglecting these variations can introduce biases in the inferred radial baryonic acceleration, ultimately affecting the shape and tightness of the relation. Given that the RAR is one of the tightest known dynamical scaling relations, its reproducibility serves as a stringent test for galaxy formation and evolution models, as they must be able to reproduce both its shape and remarkably small scatter (as well as its further 'fundamental' features identified in Stiskalek & Desmond 2023). Accurately modelling $\Upsilon_\star$ is therefore essential for placing meaningful constraints on the dynamical mass distribution of disc galaxies and the physical processes that determine galaxy dynamics.

4.3 Redshift evolution

Our sample, although small, extends to significantly higher redshifts than previous samples used to investigate the RAR. In this section, we therefore investigate whether there is any significant evidence for evolution in the RAR with redshift. To investigate potential redshift evolution in the RAR, we extend our model for the combined (with SPARC) data set by introducing a redshift-dependent acceleration scale of the form:

$$a(z) = a_0 + a_1 \times z, \tag{15}$$

where the a_1 term captures the evolution with redshift, z. We refit the RAR using this model in ROXY, and show the resulting posterior distribution of the parameters in Fig. 17.

We find a tentative evidence for evolution with $a_1 = 4.47 \pm 1.88 \times 10^{-10}$ ms^{-2}, corresponding to a 2.4 σ evidence that the acceleration scale (a_0) increases with redshift.

To explore whether this redshift evolution of the RAR could be linked to cosmological expansion (as suggested by Milgrom 2009), we compare our redshift dependent acceleration scale a_1 to the redshift-dependence of the Hubble parameter. To do so we compute $H(z)$ assuming flat ΛCDM with $\Omega_{\rm m} = 0.3$ at the
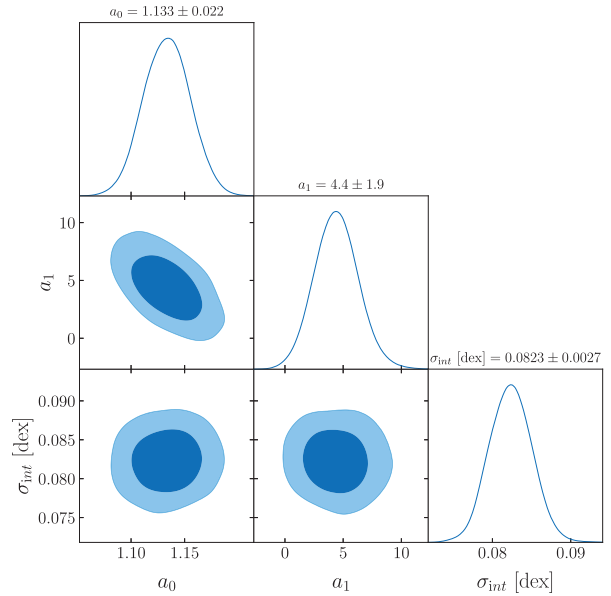
Figure 17. The corner plot showing the posterior distribution of the parameters from the redshift dependent fit to the RAR. The 2D posterior contours correspond to 68 per cent and 95 per cent confidence levels.

redshifts of our galaxies. Fitting a straight line to these points, we find $dH(z)/dz = 1.08 \times 10^{-18}$s^{-1}. To make this comparison independent of the proportionality constant, we compute the ratio a_1/a_0 from our fit and compare it with $(dH(z)/dz)/H_0$, which is $\sim$ 0.47. We find that this value is consistent with our inferred ratio $a_1/a_0 = 3.96 \pm 1.72$ at the 2σ level, suggesting that our results are consistent with $a_0(z) \propto H(z)$.

In Fig. 18, we then compare our RAR at $z = 0.5$, as shown by the blue line, with the ΛCDM expectation from the hydrodynamical simulation of Keller & Wadsley (2017), denoted by the purple shaded region. We find that our RAR at $z = 0.5$ tracks the simulation prediction reasonably well across most of the $g_{\rm bar}$ acceleration range. We also performed a similar comparison at redshift $z = 1$ and find that our predicted RAR is again consistent within the uncertainties with the Keller & Wadsley (2017) results. We caution however that
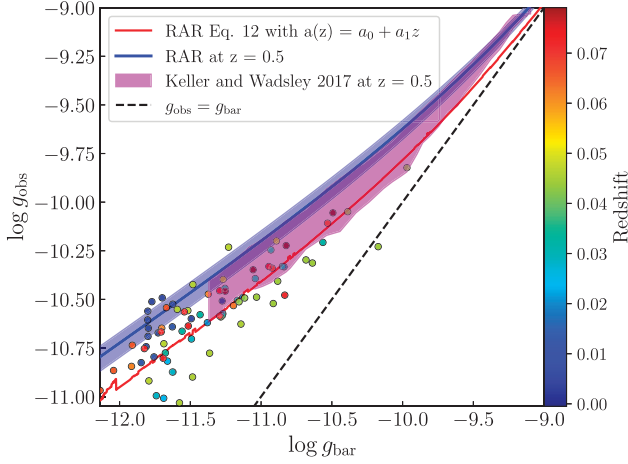
Figure 18. The extrapolated RAR at $z = 0.5$ for our sample with a varying mass-to-light ratio (colour-coded by their redshift) combined with SPARC (not shown), using a redshift dependent acceleration scale given by equation (15). The red line shows the best-fitting $z = 0$ RAR from the redshift dependent model, while the blue line corresponds to our extrapolated RAR at $z = 0.5$. The purple shaded region shows the result from the Keller & Wadsley (2017) simulations at $z = 0.5$.

this is an extreme extrapolation of a linear relation from our relatively low-redshift sample.

Such evolution should also be evident in the baryonic Tully–Fisher relation (bTFr), due to its close relation to the RAR. Ponomareva et al. (2021), using a sample of 67 galaxies at $0 < z < 0.08$ from the MIGHTEE survey, found no evidence for an evolution in the bTFr relation. Gogate et al. (2023), using a sample of H I selected galaxies in a cluster environment at $z \sim 0.2$, also found no evidence in the evolution in the normalization of the bTFr. At first glance these both appear to be evidence against the evolution in the RAR that we find. However, we note that the analysis in Ponomareva et al. (2021) did not use the SPARC data to anchor the $z \sim 0$ relation, but just used the MIGHTEE data alone to investigate the evolution, resulting in much larger uncertainties which are formally consistent with our marginal evidence for evolution in the RAR. The lack of any evidence for evolution in the sample of Gogate et al. (2023) is also statistically consistent with our results as the redshift baseline is still relatively small, alongside the relatively large uncertainties on the bTFr measurement. More recently, Jarvis et al. (2025) measured the bTFr to $z \sim 0.4$ using a sample of H I-detected galaxies within the MIGHTEE survey. They find tentative evidence that the measured bTFr for the galaxies in their sample tend to have higher velocities for a given baryonic mass compared to the $z \sim 0$ relation. This would be in line with the form of the evolution that we find. However, as explained in Jarvis et al. (2025), such an offset in the bTFr could be accounted for with a slight overabundance of molecular gas in the total baryonic mass, which is not fully accounted for. Moreover, their sample size is small (11 objects) and is dominated by galaxies with high-stellar mass $M_\star > 10^{9.8}\,\mathrm{M_\odot}$ and high baryonic mass $M_{\mathrm{bar}} > 10^{10.5}\,\mathrm{M_\odot}$, thus it is difficult to compare consistently with our results using lower mass galaxies.

A thorough investigation of this redshift dependence will require a consistent analysis of the radially varying mass-to-light ratio for all galaxies, and preferentially for those galaxies to also be selected in a consistent way. With more data in the future [from e.g. MIGHTEE and Looking at the Distant Universe with the MeerKAT Array (LADUMA; Blyth et al. 2016), and eventually the Square Kilometre

Array (SKA)], especially at higher redshift, this may provide a novel test of ΛCDM and MOND (Keller & Wadsley 2017; Hossenfelder & Mistele 2018).

4.4 The shape of the MOND interpolating function

So far we have fitted only a single MOND interpolating function (IF), the 'RAR' or 'MLS' IF of equation (12). We consider here three more general functional forms given by Famaey & McGaugh (2012):

$$g_{\mathrm{obs}} = g_{\mathrm{bar}} \left[1 - e^{-\left(\frac{g_{\mathrm{bar}}}{a_0} \right)^{\delta/2}} \right]^{-1/\delta} \tag{16a}$$

$$g_{\mathrm{obs}} = g_{\mathrm{bar}} \left(\frac{1 + \sqrt{1 + 4 \left(\frac{g_{\mathrm{bar}}}{a_0} \right)^{-n}}}{2} \right)^{\frac{1}{n}} \tag{16b}$$

$$g_{\mathrm{obs}} = g_{\mathrm{bar}} \left[\left(1 - e^{-\left(\frac{g_{\mathrm{bar}}}{a_0} \right)^{\gamma/2}} \right)^{-1/\gamma} + \left(1 - \frac{1}{\gamma} \right) e^{-\left(\frac{g_{\mathrm{bar}}}{a_0} \right)^{\gamma/2}} \right] \tag{16c}$$

These 'δ-', 'n-', and 'γ-families' contain an extra shape parameter (n, δ, γ) that describes the sharpness of transition from the Newtonian (where $g_{\mathrm{bar}} \gg a_0$) to the deep-MOND (where $g_{\mathrm{bar}} \ll a_0$) regime. This reduces to the RAR IF at $\delta = \gamma = 1$.

First, we show the constraints using the δ family from our sample only, the full SPARC sample and the Solar System quadrupole (from Desmond, Hees & Famaey 2024) in Fig. 19. We adopt uniform priors for the acceleration scale between 0.001 and 10, and for the shape δ between 0 and 30. Interestingly, our sample prefers a significantly sharper transition compared to SPARC, with a best-fitting value for δ of 3.90 ± 1.39, and a higher acceleration scale with a slightly reduced intrinsic scatter, whereas SPARC alone prefers $\delta \approx 1$ (Desmond et al. 2024).

This is an important issue because the constraint from the SPARC RAR is in $\sim 9\sigma$ tension with the inferred value of a_0 and δ from the quadrupole of the Solar System's gravitational potential, induced by the external field of the Milky Way and measured by the *Cassini* spacecraft's tracking of the ephemerides of Saturn (Desmond et al. 2024). In contrast, the constraints from our sample alone are fully consistent with this measurement, and also with the null detection of a MONDian signal in the Wide Binary Test conducted with *Gaia* data (Banik et al. 2024). This is because $\delta \gtrsim 2 - 3$ makes the Solar System and Solar neighbourhood, at $\sim 1.8\,a_0$, almost completely Newtonian. This might suggest systematics in the SPARC data resulting in an underestimate of δ, which would put MOND on a much stronger footing by removing this critical source of inconsistency. In this regard it is interesting to note that excluding the SPARC galaxies with bulges results in a best-fitting $\delta \approx 2 - 2.5$, compatible with our sample (see table 2 of Desmond et al. 2024).

4.5 Comparison with SPARC

For completeness we next consider fitting all interpolation function (IF) families to different samples, aimed at checking consistency across different acceleration regimes and data sets. In addition to the original samples, we also consider our MIGHTEE data with a constant mass-to-light ratio, $\Upsilon_K = 0.6$, as well as the low acceleration subset of SPARC, with $\log_{10}(g_{\mathrm{bar}}/\mathrm{m\,s^{-2}}) < -10$, which corresponds to the acceleration range probed by our galaxies.

To further refine the comparison between our sample and SPARC, we isolate pure disc galaxies within SPARC and apply a reduced mass-to-light ratio $\Upsilon_\star^K = 0.35$ – matching the average value preferred by our own sample – equivalent to $\Upsilon_\star^{3.6} = 0.27$ in *Spitzer*
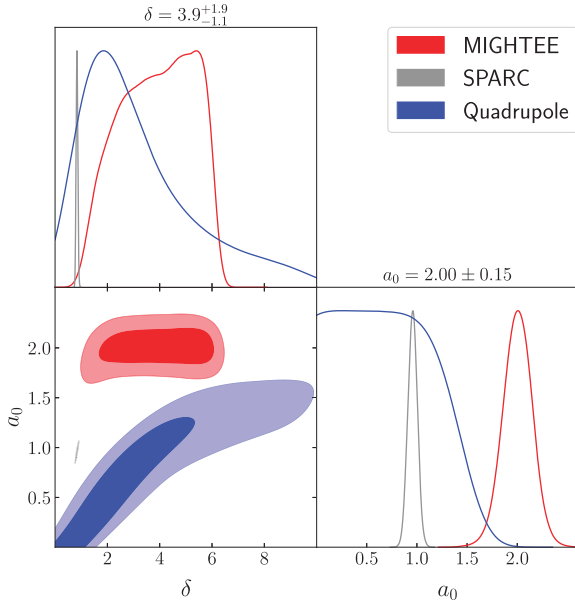
Figure 19. Posterior distributions for a_0 and δ from our sample and SPARC using the shape dependent IF described by equation (16a) and the Solar System quadrupole (Desmond et al. 2024).

3.6 μm band. We then fit this adjusted SPARC discs subset and its corresponding low acceleration portion (low acceleration SPARC discs, as per Table 4). Moreover, we repeat the analysis on two additional joint data sets: the first one – our MIGHTEE sample with a constant $\Upsilon_\star$ combined with the high acceleration portion of SPARC data, and the second one – our varying $\Upsilon_\star$ MIGHTEE sample with the high acceleration data points of the SPARC discs with reduced mass-to-light ratio.

The results for the δ family for all these cases are shown in Table 4, and the constraints from the n and γ families are presented in Table B1. These clearly show that our MIGHTEE sample alone prefers a higher acceleration scale, steeper shape parameter $\gtrsim 2$ and smaller intrinsic scatter than either the SPARC data set (or any subset of it), or any of variant of the combined data sets. The SPARC data prefers $\delta \approx 1$ in all cases, which is not consistent with the Solar System tests mentioned above in a MONDian interpretation. Reducing the SPARC mass-to-light ratio to match our sample does not reconcile the discrepancy in the inferred parameters (a_0, δ, σ_{int}) between SPARC and our data – or with Solar System constraints. In fact, it leads to even lower inferred values for the acceleration scale a_0 and shape parameter δ and increases the intrinsic scatter to ~ 0.1

dex. Likewise, combining MIGHTEE (regardless of the $\Upsilon_\star$ model) with the full SPARC sample or pure SPARC discs fails to alleviate the tension. Neither adjusting the global $\Upsilon_\star$ in SPARC nor restricting the analysis to its low-acceleration regime brings the SPARC-derived constraints closer to those from MIGHTEE. Similarly, modifying our own sample (by adopting a fixed mass-to-light ratio of 0.6) does not significantly alter the shape parameter δ. These findings suggest that the discrepancy is not solely due to the mass-to-light ratios (or their radial variations), but is intrinsic to the data used. It may be because the MIGHTEE data is a homogeneous sample, whereas SPARC comprises a heterogeneous compilation of galaxies.

5 SUMMARY AND CONCLUSIONS

In this paper, we perform an analysis of the radial acceleration relation in 19 rotationally supported galaxies by leveraging the homogeneous sample of H I-selected galaxies from the MIGHTEE-H I survey, with spatially resolved H I kinematics and homogeneously analysed photometry from SED fitting across 10 optical and near-infrared bands. The aim of this study was to investigate the RAR using a novel approach – resolved stellar mass modelling from SED fitting, extending to a low-mass, homogeneously selected H I-galaxies, whilst increasing the redshift range to $z \sim 0.08$.

We perform resolved SED fitting in the optical and near-infrared to measure the radial mass-to-light ratio variations across our galaxies. Using these variations, we derive the stellar surface densities, which, combined with the gas surface densities, allow us to determine the radial acceleration due to baryons. Our results reveal a tight RAR with an acceleration scale $a_0 = 1.69 \pm 0.13 \times 10^{-10}$ m s^{-2}, higher than previously reported for the SPARC galaxies alone, and with an intrinsic scatter of $\sigma_{int} = 0.045 \pm 0.022$ dex. We also explore the impact of adopting a constant mass-to-light ratio versus one that varies across the galaxy sample compared to our initial approach of varying mass-to-light ratio. We find that adopting a spatially varying mass-to-light ratio yields the tightest RAR, suggesting that at least within the low-acceleration regime, this becomes increasingly important. We also combine our sample with the high acceleration portion of the SPARC RAR data and fit the same functional form, yielding a lower acceleration scale of $a_0 = 1.32 \pm 0.13$ m s^{-2}. However, the combined best-fitting RAR is in tension with the trend preferred by our data alone at the 2σ level. This is not unsurprising, as this tension highlights the critical role of adopting an appropriate mass-to-light ratio, particularly in the low acceleration regime. Different assumptions on the $\Upsilon_\star$ ratio can lead to significant discrepancies in the inferred RAR. This is particularly relevant in the context of constraining dark-matter halo profiles – where an incorrect $\Upsilon_\star$

Table 4. Constraints on the RAR parameters a_0 (acceleration scale), σ_{int} (intrinsic scatter), and sharpness of transition (Shape) for the more general δ-family of interpolating functions. We show various data combinations and mass-to-light models to investigate the cause of the differences between the constraints from the MIGHTEE and SPARC samples (see Section 4.5).

Sample	MIGHTEE $\Upsilon_\star$	SPARC $\Upsilon_\star$	a_0	Shape δ	σ_{int}
MIGHTEE	Varying Υ_K	–	2.00 ± 0.15	3.94 ± 1.4	0.043 ± 0.021
MIGHTEE	$\Upsilon_K = 0.6$	–	1.48 ± 0.095	4.85 ± 1.21	0.032 ± 0.020
SPARC	–	$\Upsilon_{\star,disc} = 0.5, \Upsilon_{\star,bulge} = 0.7$	0.96 ± 0.05	0.84 ± 0.03	0.081 ± 0.003
SPARC discs	–	$\Upsilon_{\star,disc} = 0.27$	0.22 ± 0.06	0.34 ± 0.02	0.102 ± 0.004
Low acceleration SPARC	–	$\Upsilon_{\star,disc} = 0.5, \Upsilon_{\star,bulge} = 0.7$	0.85 ± 0.06	0.75 ± 0.03	0.084 ± 0.003
Low acceleration SPARC discs	–	$\Upsilon_{\star,disc} = 0.27$	0.20 ± 0.06	0.32 ± 0.02	0.103 ± 0.004
MIGHTEE + high acceleration SPARC	Varying Υ_K	$\Upsilon_{\star,disc} = 0.5, \Upsilon_{\star,bulge} = 0.7$	1.76 ± 0.15	1.29 ± 0.11	0.061 ± 0.006
MIGHTEE + high acceleration SPARC	$\Upsilon_K = 0.6$	$\Upsilon_{\star,disc} = 0.5, \Upsilon_{\star,bulge} = 0.7$	1.27 ± 0.12	1.12 ± 0.09	0.049 ± 0.010
MIGHTEE + high acceleration SPARC discs	Varying Υ_K	$\Upsilon_{\star,disc} = 0.27$	0.81 ± 0.21	0.48 ± 0.05	0.028 ± 0.017

assumption could systematically bias the interpretation of the scaling relation and lead to discrepancies in the inferred dark matter distributions – or in testing theories of modified gravity such as MOND. The comparison of different $\Upsilon_\star$ prescriptions underscores that using a spatially resolved approach provides the tightest correlation with the smallest intrinsic scatter in the RAR. We also fit a double power law to our data. Although our limited sample size does not justify a more complicated parametrization, combining our data with the SPARC high acceleration sample, we find that such a parametrization is preferred. This suggests that the more flexible functional form better accommodates the diversity of baryonic accelerations in such a large data set. Interestingly, for both our sample alone and the combined data set, the slope of the double power-law fit in the low acceleration regime of $\beta \sim 0.5$ is consistent with MOND predictions; however, this does not rule out consistency with ΛCDM.

We also perform the first measurement of the potential evolution in the RAR with redshift. Although our sample size is small, we find tentative evidence for redshift evolution at the 2.4σ level. However, such an evolution would need to be confirmed with a much larger sample, preferably extending to higher redshifts, but analysed in a consistent manner following the work presented here.

In addition, we consider a generalized interpolating function of the δ family. We find a sharper transition from the Newtonian to the deep MOND regime, compared to previous SPARC studies, with a shape δ of 3.90 ± 1.39, and a higher acceleration scale with a slightly reduced intrinsic scatter. Interestingly, this has much greater consistency with constraints on MOND from the Solar System quadrupole (Desmond et al. 2024) and wide binary test (Banik et al. 2024). We further examine the n and γ IF families with similar results. In each case we find that using a varying mass-to-light ratio results in a higher a_0 than when one adopts a single value of $\Upsilon_\star = 0.6$. This again emphasizes the need for accurate measurements of the mass-to-light ratio, particularly in the low-acceleration regime in order to probe MONDian theories.

The uniqueness of this study resides in the fact that we probe the low acceleration regime, which is often more challenging due to observational limitations, by using a homogeneously analysed sample. Unlike previous studies, which primarily focused on local galaxies, our method also extends the analysis to higher redshift using a multiwavelength approach, providing a more comprehensive view of the RAR across cosmic time. This is particularly relevant for future H I surveys with the SKA, where improved spatial resolution, better sensitivity, and sky coverage will allow for even deeper investigations into the disc–halo relation towards higher redshifts. Furthermore, incorporating other emission line tracers, such as CO, ionized gas Hα, and stellar kinematics, can aid in constraining the rotation curves in the inner parts of disc galaxies, whilst also providing a direct measurement of their contribution to the baryonic mass, where accurately mapping the dark matter and baryonic distributions are crucial in mitigating the disc–halo degeneracy.

Ultimately, our work emphasizes the necessity of accurately determining the mass-to-light ratios using deep multiwavelength observations for constraining the dark matter and baryonic distributions, expanding towards homogeneously selected samples beyond the local Universe. This not only enables tests of cosmic evolution but also helps mitigate systematics that affect local samples, such as peculiar velocities and uncertainties in distance estimates. Future advancements, including higher resolution H I data and combined optical emission line tracers (CO, Hα), will be crucial in refining our understanding of galaxy formation and evolution and constraining the dark matter properties of galaxies.

DATA AVAILABILITY

The MIGHTEE-H I spectral cubes are available from https://doi.org/10.48479/jkc0-g916 (Heywood et al. 2024). The optical and near-infrared data used to measure the stellar surface brightness properties of the galaxies are all in the public domain. Other data underlying the article are available on request to the corresponding author.

REFERENCES

Adams N. J., Bowler R. A. A., Jarvis M. J., Varadaraj R. G., Häußler B., 2023, MNRAS, 523, 327

Aihara H. et al., 2018, PASJ, 70, S4

Aihara H. et al., 2019, PASJ, 71, 114

Aihara H. et al., 2022, PASJ, 74, 247

Bacchini C., Fraternali F., Iorio G., Pezzulli G., 2019, A&A, 622, A64

Banik I., Pittordis C., Sutherland W., Famaey B., Ibata R., Mieske S., Zhao H., 2024, MNRAS, 527, 4573

Bartlett D. J., Desmond H., 2023, preprint (arXiv:2309.00948)

Bell E. F., de Jong R. S., 2001, ApJ, 550, 212

Bell E. F., McIntosh D. H., Katz N., Weinberg M. D., 2003, ApJS, 149, 289

Bershady M. A., Verheijen M. A. W., Westfall K. B., Andersen D. R., Swaters R. A., Martinsson T., 2010, ApJ, 716, 234

Bingham E. et al., 2018, preprint (arXiv:1810.09538)

Blyth S. et al., 2016, in Proc. MeerKAT Sci.: On the Pathway to the SKA. SISSA, Trieste, PoS#004

Bosma A., 1978, PhD thesis, University of Groningen, Netherlands

Boylan-Kolchin M., Bullock J. S., Kaplinghat M., 2011, MNRAS, 415, L40

Boylan-Kolchin M., Bullock J. S., Kaplinghat M., 2012, MNRAS, 422, 1203

Bradley L. et al., 2024, astropy/photutils: 1.12.0, Zenodo, available in https://zenodo.org/records/10967176

Brouwer M. M. et al., 2021, A&A, 650, A113

Bruzual G., Charlot S., 2003, MNRAS, 344, 1000

Bullock J. S., Boylan-Kolchin M., 2017, ARA&A, 55, 343

Calzetti D., Armus L., Bohlin R. C., Kinney A. L., Koornneef J., Storchi-Bergmann T., 2000, ApJ, 533, 682

Caon N., Capaccioli M., D'Onofrio M., 1993, MNRAS, 265, 1013

Capaccioli M., 1989, in Corwin Harold G. J., Bottinelli L., eds, World of Galaxies (Le Monde des Galaxies). Springer-Verlag, Berlin, p. 208

Cardelli J. A., Clayton G. C., Mathis J. S., 1989, ApJ, 345, 245

Carnall A. C., McLure R. J., Dunlop J. S., Davé R., 2018, MNRAS, 480, 4379

Catinella B. et al., 2018, MNRAS, 476, 875

Chabrier G., 2003, PASP, 115, 763

Chae K.-H., Lelli F., Desmond H., McGaugh S. S., Li P., Schombert J. M., 2020, ApJ, 904, 51

Chae K.-H., Desmond H., Lelli F., McGaugh S. S., Schombert J. M., 2021, ApJ, 921, 104

Chae K.-H., Lelli F., Desmond H., McGaugh S. S., Schombert J. M., 2022, Phys. Rev. D, 106, 103025

Chan M. H., Del Popolo A., 2020, MNRAS, 492, 5865

Charlot S., Fall S. M., 2000, ApJ, 539, 718

Cuddeford P., 1993, MNRAS, 262, 1076

Cuillandre J.-C. J. et al., 2012, in Peck A. B., Seaman R. L., Comeron F., eds, Proc. SPIE Conf. Ser. Vol. 8448, Observatory Operations: Strategies, Processes, and Systems IV. SPIE, Bellingham, p. 84480M

Desmond H., 2017, MNRAS, 464, 4160

Desmond H., 2023, MNRAS, 526, 3342

Desmond H., Bartlett D. J., Ferreira P. G., 2023, MNRAS, 521, 1817

Desmond H., Hees A., Famaey B., 2024, MNRAS, 530, 1781

Di Teodoro E. M., Fraternali F., 2015, MNRAS, 451, 3021

Dutton A. A., Macciò A. V., Obreja A., Buck T., 2019, MNRAS, 485, 1886

Famaey B., McGaugh S. S., 2012, Living Rev. Relat., 15, 10

Fitzpatrick E. L., 1999, PASP, 111, 63

Flores R. A., Primack J. R., 1994, ApJ, 427, L1

Fouque P., Bottinelli L., Gouguenheim L., Paturel G., 1990, ApJ, 349, 1

Freundlich J., Famaey B., Oria P.-A., Bílek M., Müller O., Ibata R., 2022, A&A, 658, A26

Garaldi E., Romano-Díaz E., Porciani C., Pawlowski M. S., 2018, Phys. Rev. Lett., 120, 261301

Garrison-Kimmel S., Rocha M., Boylan-Kolchin M., Bullock J. S., Lally J., 2013, MNRAS, 433, 3539

Gogate A. R., Verheijen M. A. W., van der Hulst J. M., Jaffé Y. L., 2023, MNRAS, 519, 4279

Hale C. L. et al., 2025, MNRAS, 536, 2187

Handley W., 2018, J. Open Source Softw., 3, 849

Heywood I. et al., 2022, MNRAS, 509, 2150

Heywood I. et al., 2024, MNRAS, 534, 76

Hossenfelder S., Mistele T., 2018, Int. J. Mod. Phys. D, 27, 1847010

Into T., Portinari L., 2013, MNRAS, 430, 2715

Iorio G., 2018, Phd thesis, University of Bologna, Italy

Iorio G., Fraternali F., Nipoti C., Di Teodoro E., Read J. I., Battaglia G., 2017, MNRAS, 466, 4159

Jarvis M. et al., 2016, in Proc. MeerKAT Sci.: On the Pathway to the SKA. SISSA, Trieste, PoS#006

Jarvis M. J. et al., 2025, preprint (arXiv:2506.11935)

Jedrzejewski R. I., 1987, MNRAS, 226, 747

Józsa G. I. G., Kenn F., Oosterloo T. A., Klein U., 2012, Astrophysics Source Code Library, record ascl:1208.008

Keller B. W., Wadsley J. W., 2017, ApJ, 835, L17

Klypin A., Kravtsov A. V., Valenzuela O., Prada F., 1999, ApJ, 522, 82

Lange J. U., 2023, MNRAS, 525, 3181

Lelli F., McGaugh S. S., Schombert J. M., 2016, AJ, 152, 157

Lelli F., McGaugh S. S., Schombert J. M., Pawlowski M. S., 2017, ApJ, 836, 152

Lelli F., McGaugh S. S., Schombert J. M., Desmond H., Katz H., 2019, MNRAS, 484, 3267

Leroy A. K., Walter F., Brinks E., Bigiel F., de Blok W. J. G., Madore B., Thornley M. D., 2008, AJ, 136, 2782

Li P., Lelli F., McGaugh S., Schombert J., 2018, A&A, 615, A3

Liang Y., Xu D., Sluse D., Sonnenfeld A., Shu Y., 2025, MNRAS, 536, 2672

Ludlow A. D. et al., 2017, Phys. Rev. Lett., 118, 161103

Maddox N. et al., 2021, A&A, 646, A35

Mancera Piña P. E. et al., 2020, MNRAS, 495, 3636

Mancera Piña P. E., Posti L., Fraternali F., Adams E. A. K., Oosterloo T., 2021, A&A, 647, A76

Mancera Piña P. E., Fraternali F., Oosterloo T., Adams E. A. K., di Teodoro E., Bacchini C., Iorio G., 2022, MNRAS, 514, 3329

Mancera Piña P. E., Read J. I., Kim S., Marasco A., Benavides J. A., Glowacki M., Pezzulli G., Lagos C. d. P., 2025, preprint (arXiv:2505.22727)

Marasco A., Fall S. M., Di Teodoro E. M., Mancera Piña P. E., 2025, A&A, 695, L23

Martinsson T. P. K., Verheijen M. A. W., Westfall K. B., Bershady M. A., Andersen D. R., Swaters R. A., 2013, A&A, 557, A131

McCracken H. J. et al., 2012, A&A, 544, A156

McGaugh S. S., 2004, ApJ, 609, 652

McGaugh S. S., 2005, Phys. Rev. Lett., 95, 171302

McGaugh S. S., 2012, AJ, 143, 40

McGaugh S. S., Schombert J. M., 2015, ApJ, 802, 18

McGaugh S. S., Schombert J. M., Bothun G. D., de Blok W. J. G., 2000, ApJ, 533, L99

McGaugh S. S., Lelli F., Schombert J. M., 2016, Phys. Rev. Lett., 117, 201101

McGaugh S. S., Schombert J. M., Lelli F., 2017, ApJ, 851, 22

McGaugh S. S., Lelli F., Schombert J. M., 2020, Res. Notes Am. Astron. Soc., 4, 45

Meidt S. E. et al., 2014, ApJ, 788, 144

Mercado F. J., Bullock J. S., Moreno J., Boylan-Kolchin M., Hopkins P. F., Wetzel A., Faucher-Giguère C.-A., Samuel J., 2024, MNRAS, 530, 1349

Meyer M., Robotham A., Obreschkow D., Westmeier T., Duffy A. R., Staveley-Smith L., 2017, Publ. Astron. Soc. Aust., 34, 52

Milgrom M., 1983, ApJ, 270, 371

Milgrom M., 2009, ApJ, 698, 1630

Mistele T., McGaugh S., Lelli F., Schombert J., Li P., 2024, J. Cosmol. Astropart. Phys., 2024, 020

Mobasher B. et al., 2015, ApJ, 808, 101

Moore B., 1994, Nature, 370, 629

Moore B., Quinn T., Governato F., Stadel J., Lake G., 1999, MNRAS, 310, 1147

Navarro J. F., Benítez-Llambay A., Fattahi A., Frenk C. S., Ludlow A. D., Oman K. A., Schaller M., Theuns T., 2017, MNRAS, 471, 1841

Norris M. A., Meidt S., Van de Ven G., Schinnerer E., Groves B., Querejeta M., 2014, ApJ, 797, 55

Paranjape A., Sheth R. K., 2021, MNRAS, 507, 632

Phan D., Pradhan N., Jankowiak M., 2019, preprint (arXiv:1912.11554)

Ponomareva A. A., Verheijen M. A. W., Papastergis E., Bosma A., Peletier R. F., 2018, MNRAS, 474, 4366

Ponomareva A. A. et al., 2021, MNRAS, 508, 1195

Prugniel P., Simien F., 1997, A&A, 321, 111

Röck B., Vazdekis A., Peletier R. F., Knapen J. H., Falcón-Barroso J., 2015, MNRAS, 449, 2853

Rubin V. C., Ford W. K., Jr, Thonnard N., 1978, ApJ, 225, L107

Saintonge A., Catinella B., 2022, ARA&A, 60, 319

Saintonge A. et al., 2016, MNRAS, 462, 1749

Sanders R. H., 1990, A&AR, 2, 1

Schlegel D. J., Finkbeiner D. P., Davis M., 1998, ApJ, 500, 525

Schombert J., McGaugh S., 2014, Publ. Astron. Soc. Aust., 31, e036

Sersic J. L., 1968, Atlas de Galaxias Australes. Observatorio Astronomico, Cordoba, Argentina

Sorce J. G. et al., 2013, ApJ, 765, 94

Stiskalek R., Desmond H., 2023, MNRAS, 525, 6130

Taylor A. R. et al., 2024, MNRAS, 528, 2511

Tenneti A., Mao Y.-Y., Croft R. A. C., Di Matteo T., Kosowsky A., Zago F., Zentner A. R., 2018, MNRAS, 474, 3125

Tian Y., Umetsu K., Ko C.-M., Donahue M., Chiu I. N., 2020, ApJ, 896, 70

Tian Y., Ko C.-M., Li P., McGaugh S., Poblete S. L., 2024, A&A, 684, A180

Tiley A. L. et al., 2016, MNRAS, 460, 103

Topal S., Bureau M., Tiley A. L., Davis T. A., Torii K., 2018, MNRAS, 479, 3319

Tudorache M. N. et al., 2024, preprint (arXiv:2411.14940)

Tully R. B., Fisher J. R., 1977, A&A, 54, 661

Übler H. et al., 2017, ApJ, 842, 121

van den Bergh S., 2001, in Martínez V. J., Trimble V., Pons-Bordería M. J., eds, ASP Conf. Ser. Vol. 252, Historical Development of Modern Cosmology. Astron. Soc. Pac., San Francisco, p. 75

van der Kruit P. C., 1988, A&A, 192, 117

van der Kruit P. C., Freeman K. C., 2011, ARA&A, 49, 301

Verbeke R., Papastergis E., Ponomareva A. A., Rathi S., De Rijcke S., 2017, A&A, 607, A13

Verheijen M. A. W., 2001, ApJ, 563, 694

Virtanen P. et al., 2020, Nature Methods, 17, 261

Young J. S., Scoville N. Z., 1991, ARA&A, 29, 581

APPENDIX A: RADIAL MASS TO LIGHT RATIO VARIATIONS

Each figure below shows, on the left, the *G*-band image of the galaxy with ellipses spaced every 5 arcsec. On the right, the top panel displays the stellar surface mass density profile inferred from resolved SED fitting (in blue), with the K_s-band surface brightness profiles overlaid in red for comparison. The bottom panel shows the corresponding radial variations in the K_s-band mass-to-light ratio, Υ_K.
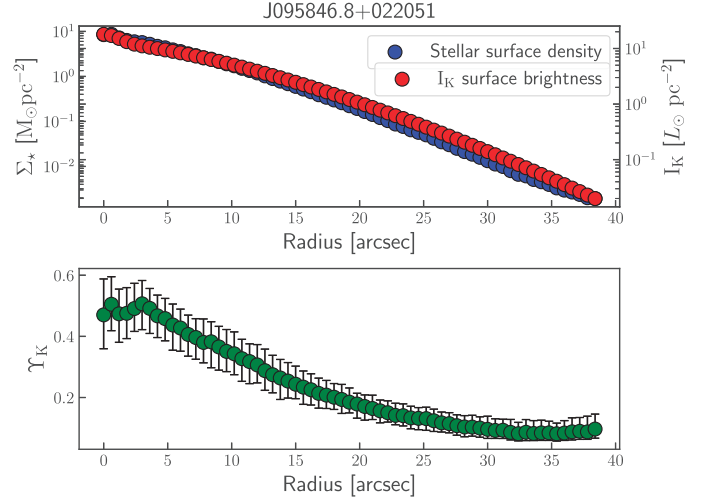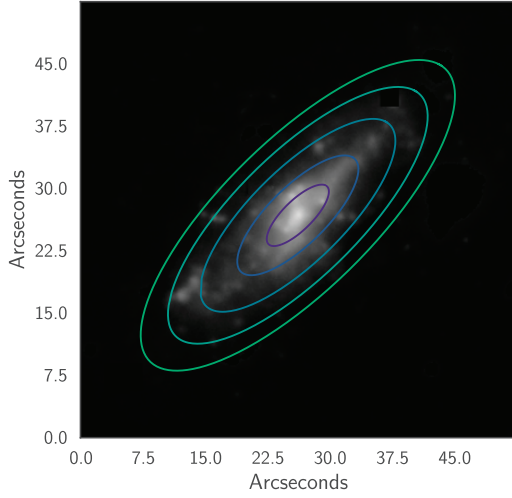
Figure A1. J095846.8+022051.
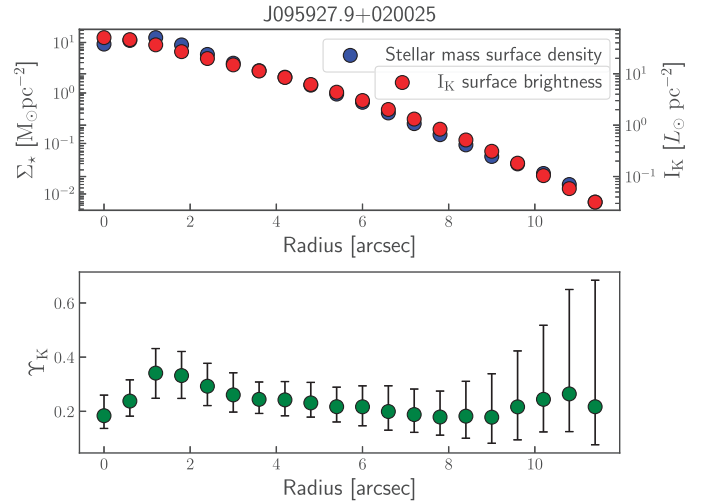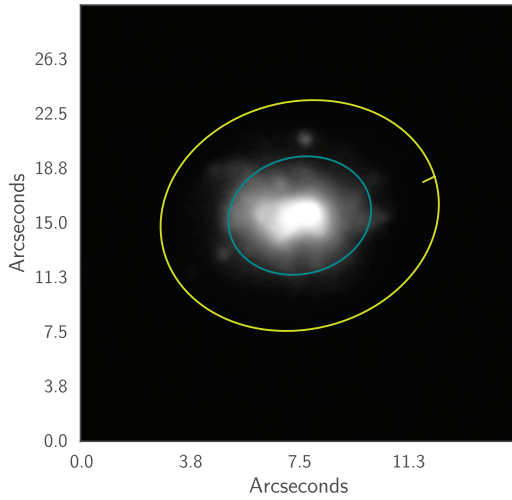
Figure A2. J095927.9+020025.
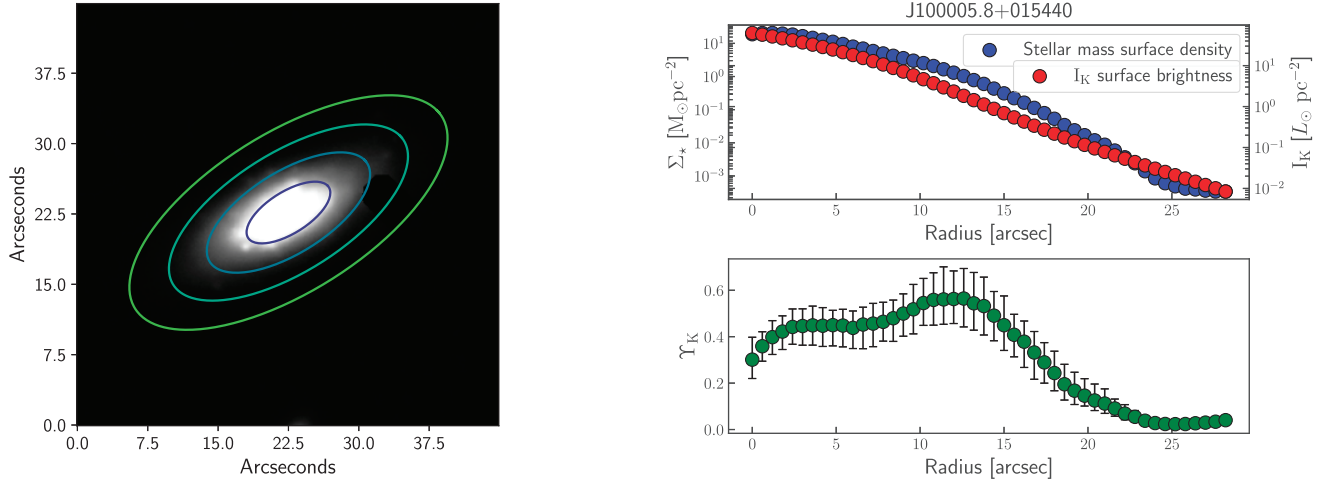
Figure A3. J100005.8+015440.
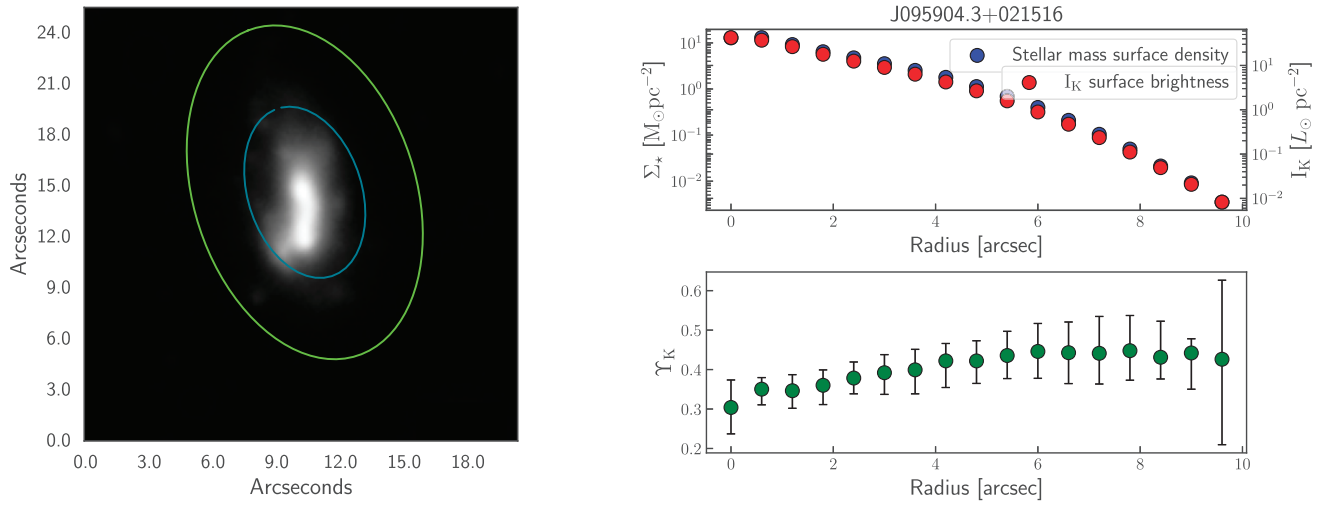
Figure A4. J095904.3+021516.
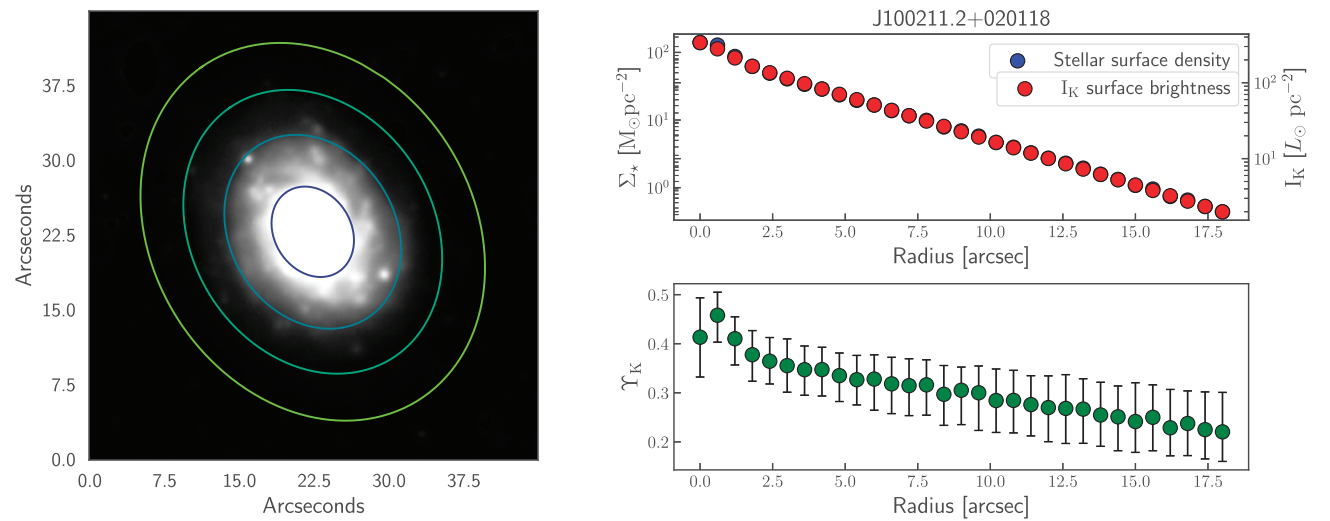
Figure A5. J100211.2+020118.
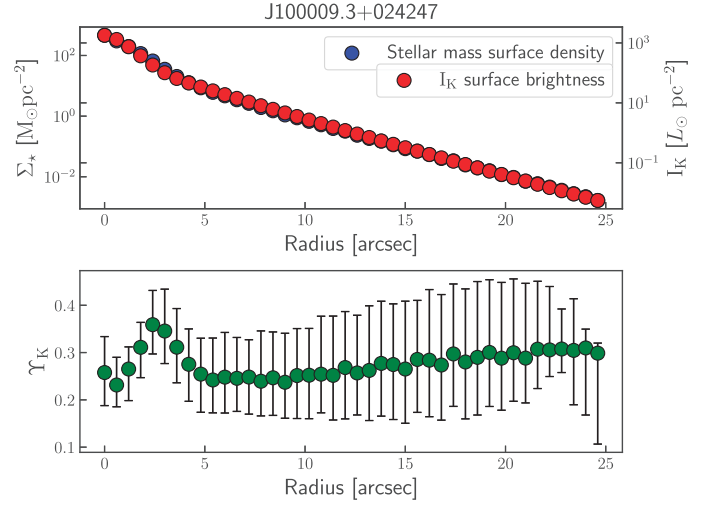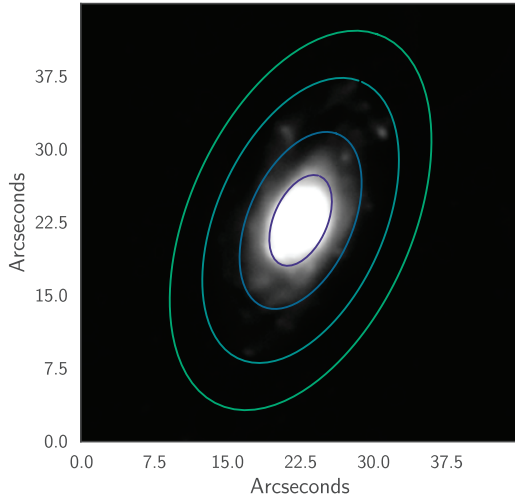
Figure A6. J100009.3+024247.
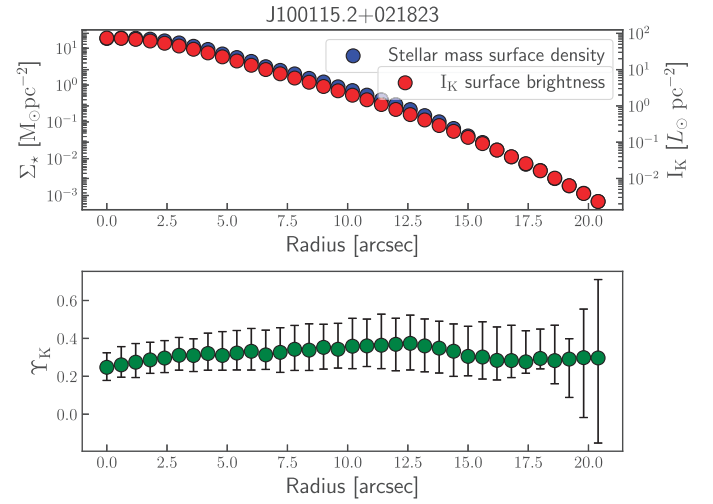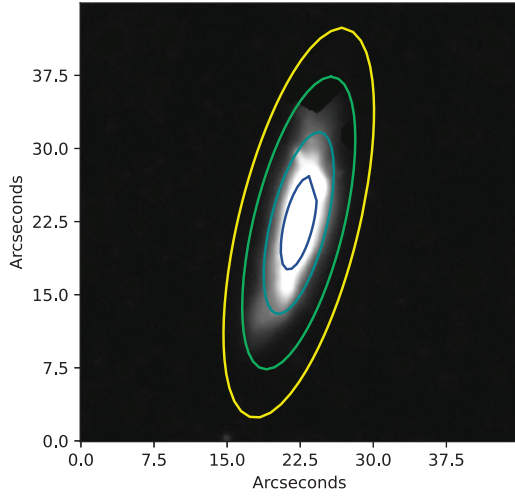
Figure A7. J100115.2+021823.
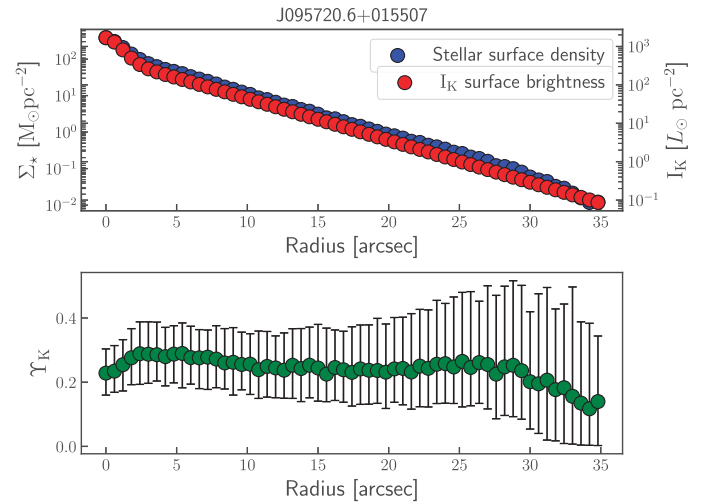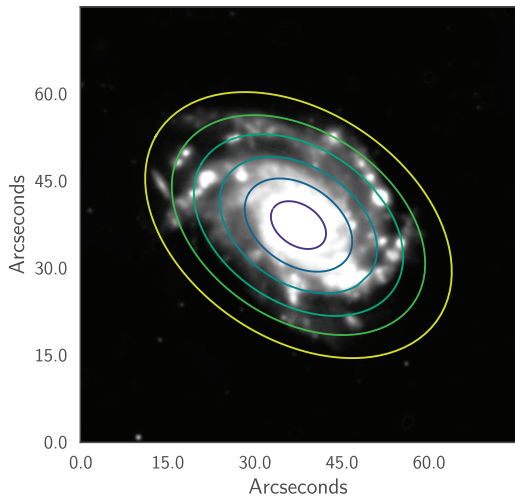
Figure A8. J095720.6+015507.
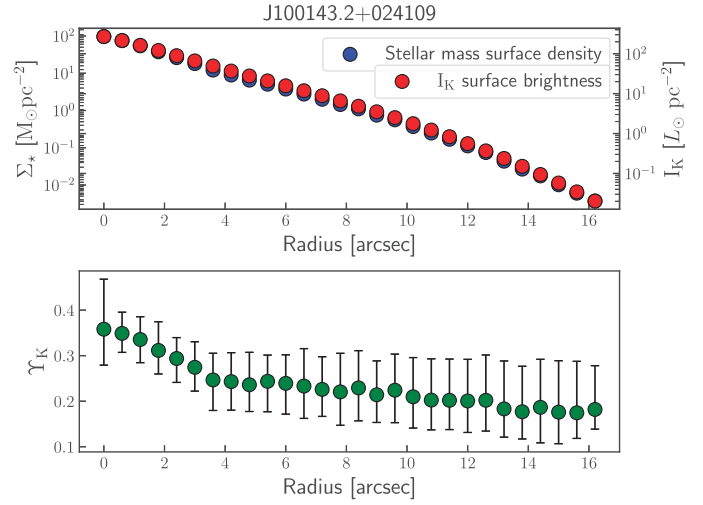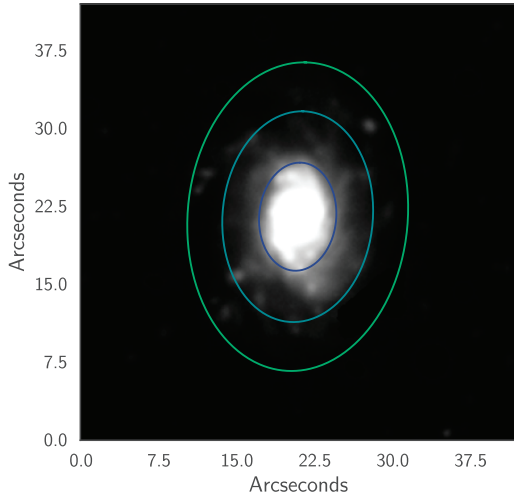
Figure A9. J100143.2+024109.
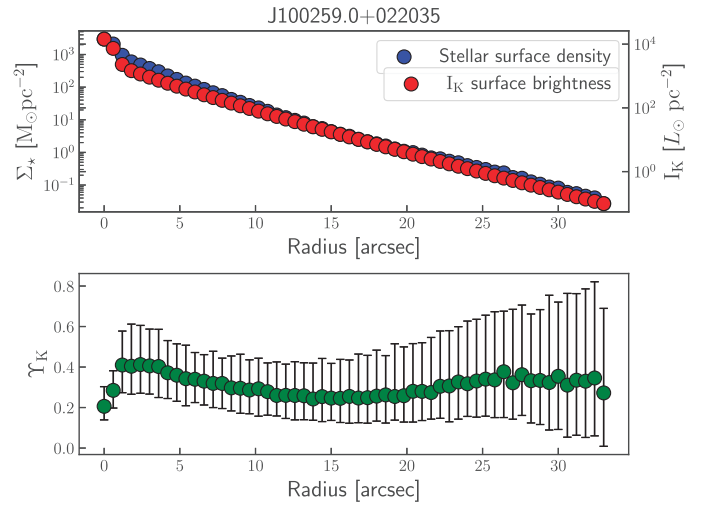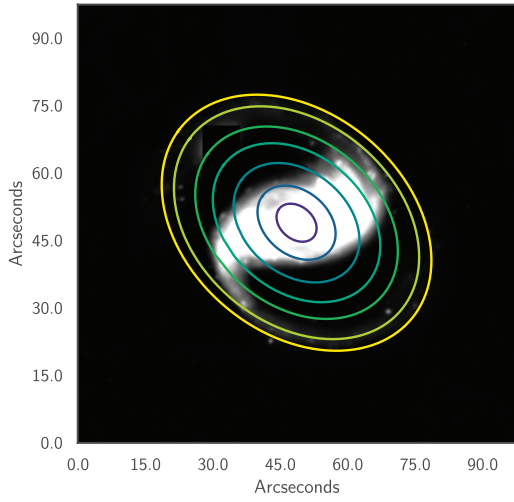
Figure A10. J100259.0+022035.
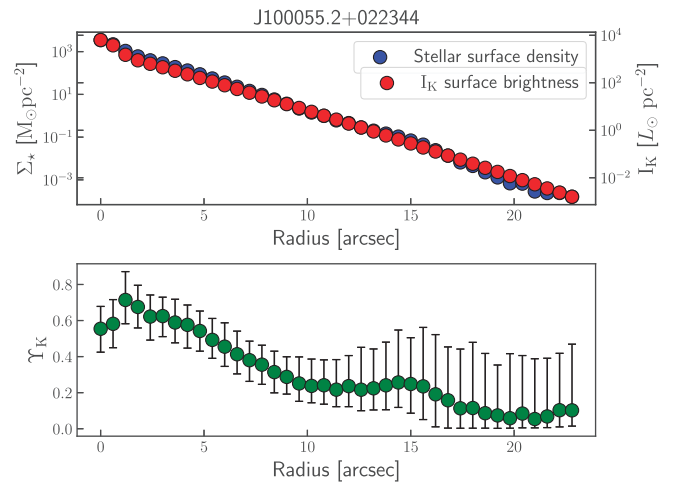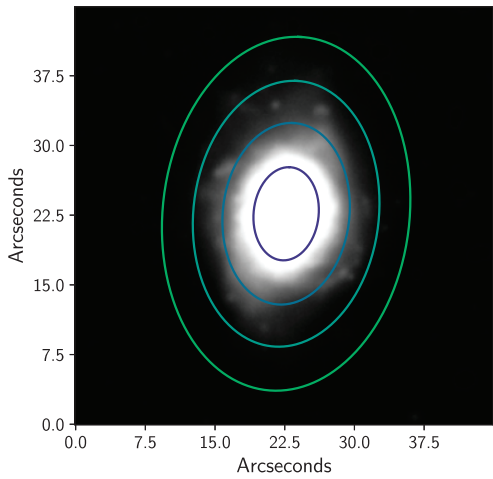
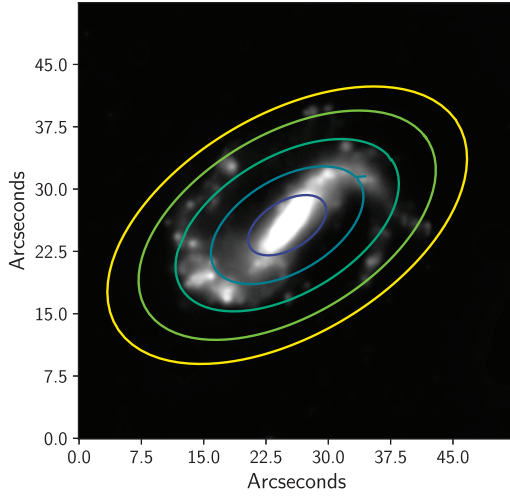**Figure A11.** J100055.2+022344.
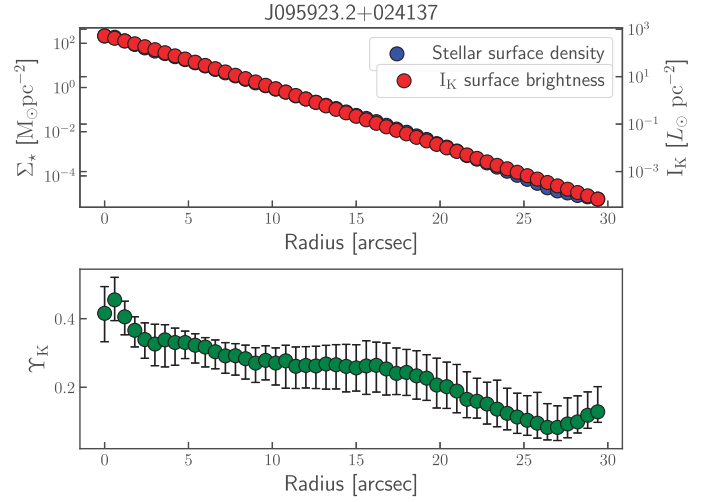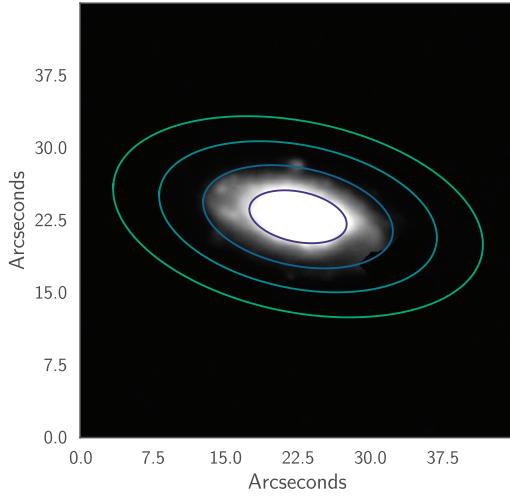
Figure A12. J095923.2+024137.
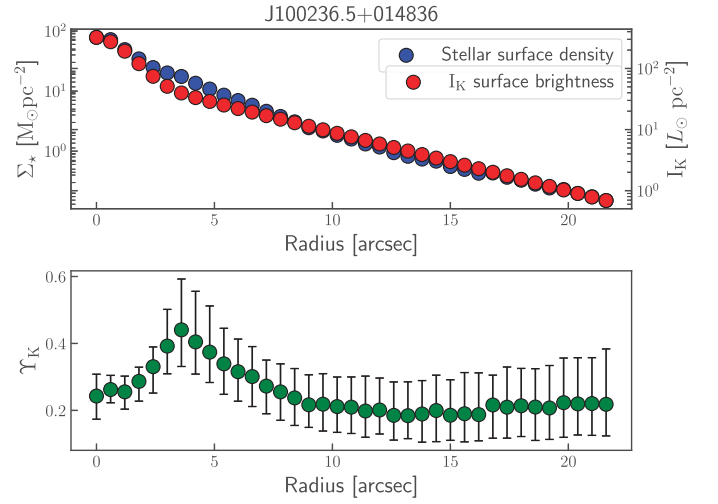
Figure A13. J100236.5+014836.
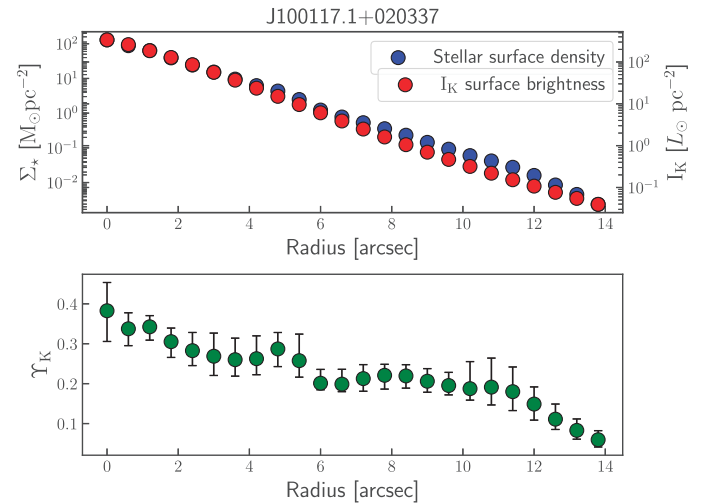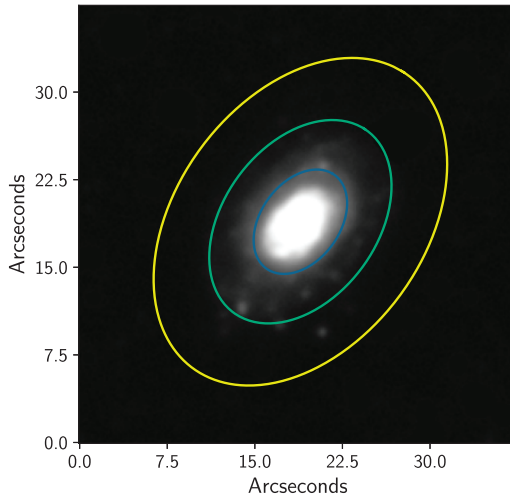
Figure A14. J100117.1+020337.
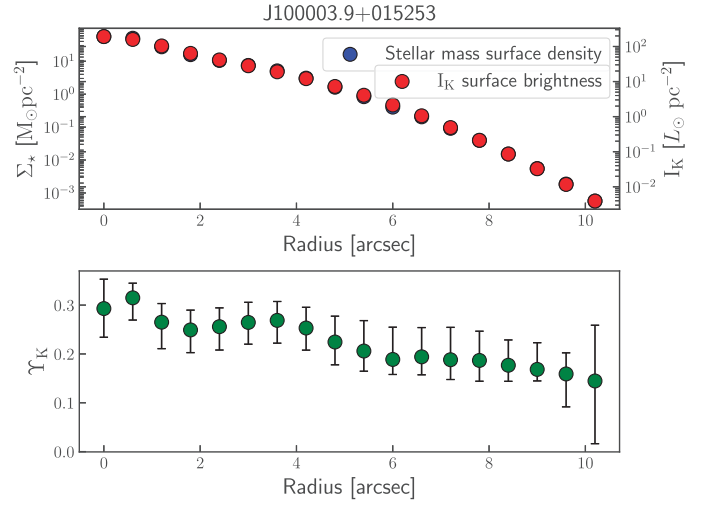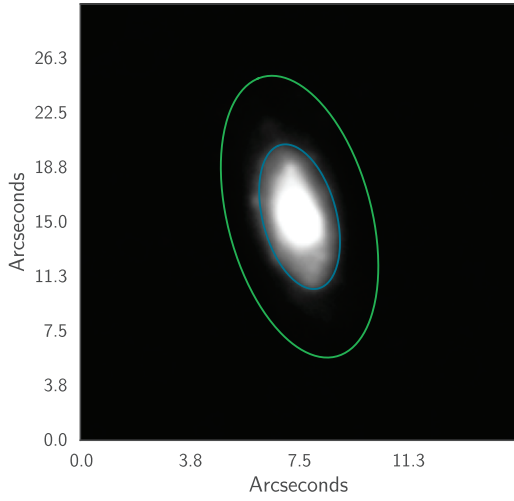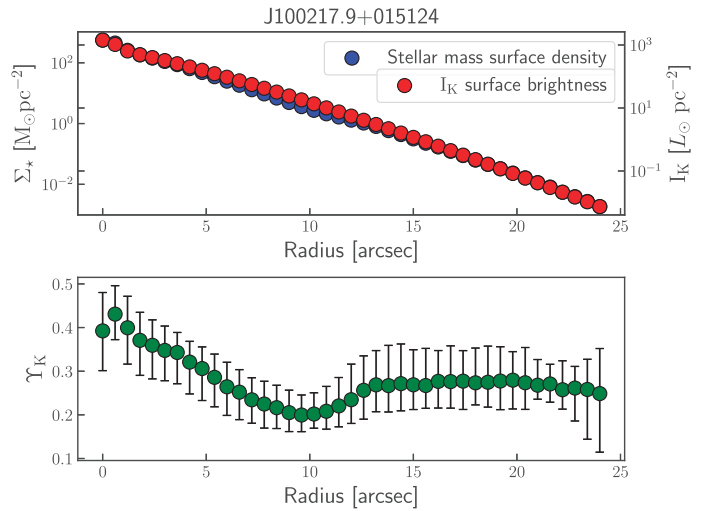
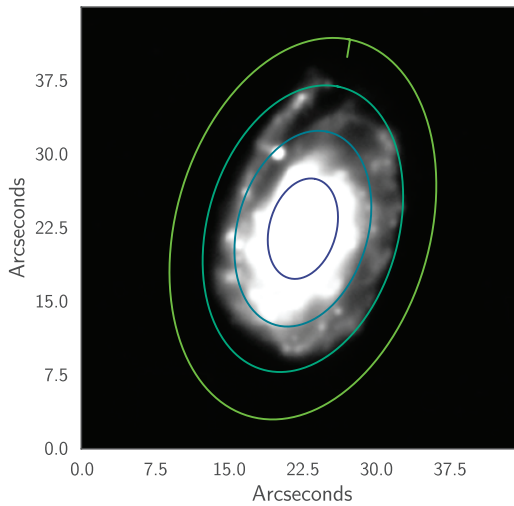**Figure A15.** J100003.9+015253.
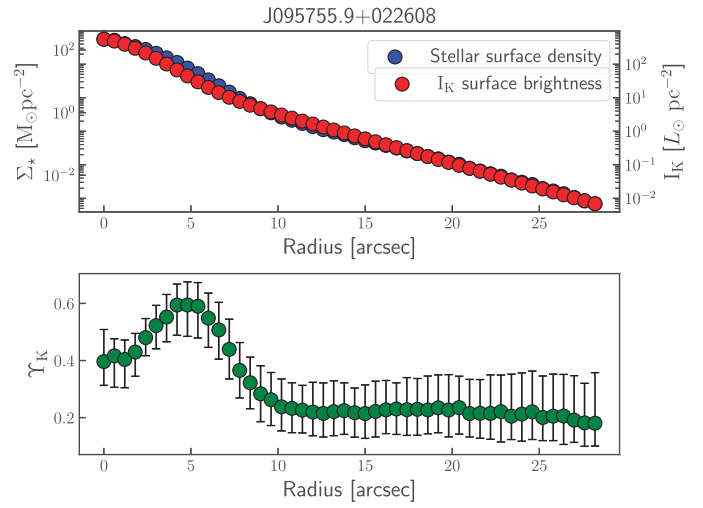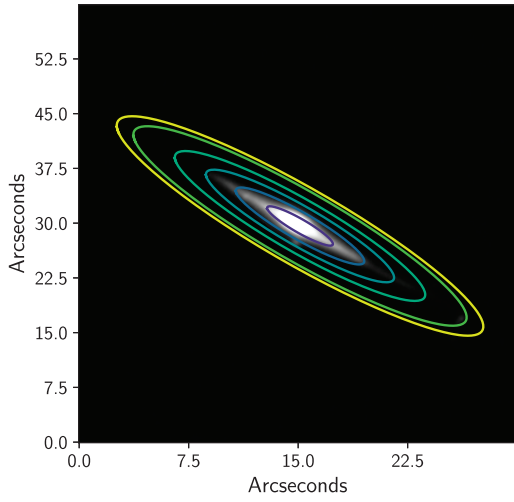
Figure A16. J095755.9+022608.

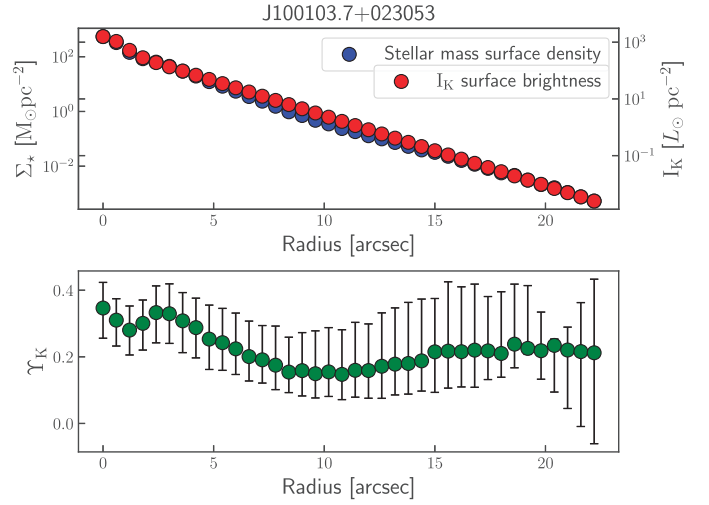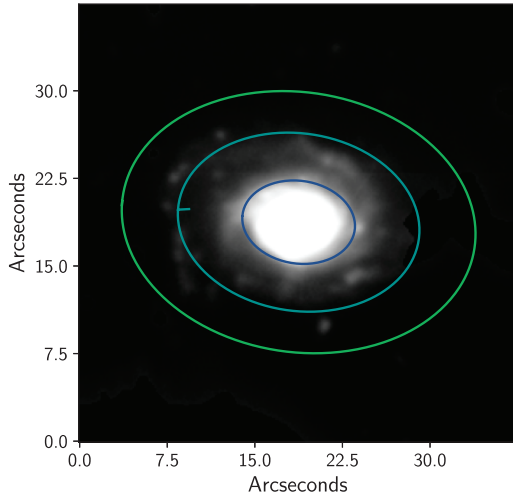**Figure A17.** J100217.9+015124.

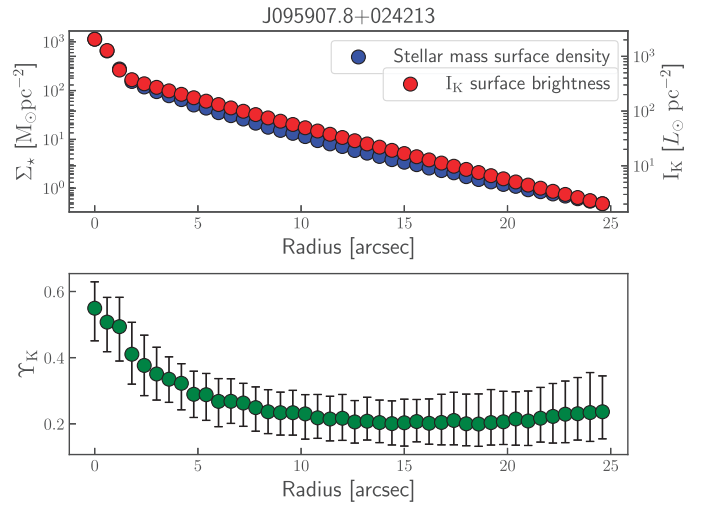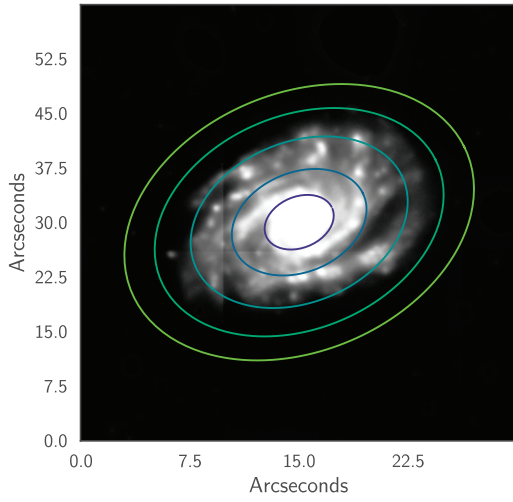**Figure A18.** J100103.7+023053.

Figure A19. J095907.8+024213.

APPENDIX B: RAR FITS

We show in Figs B1 and B2 the constraints on the parameters of the
RAR and double power-law fits respectively.

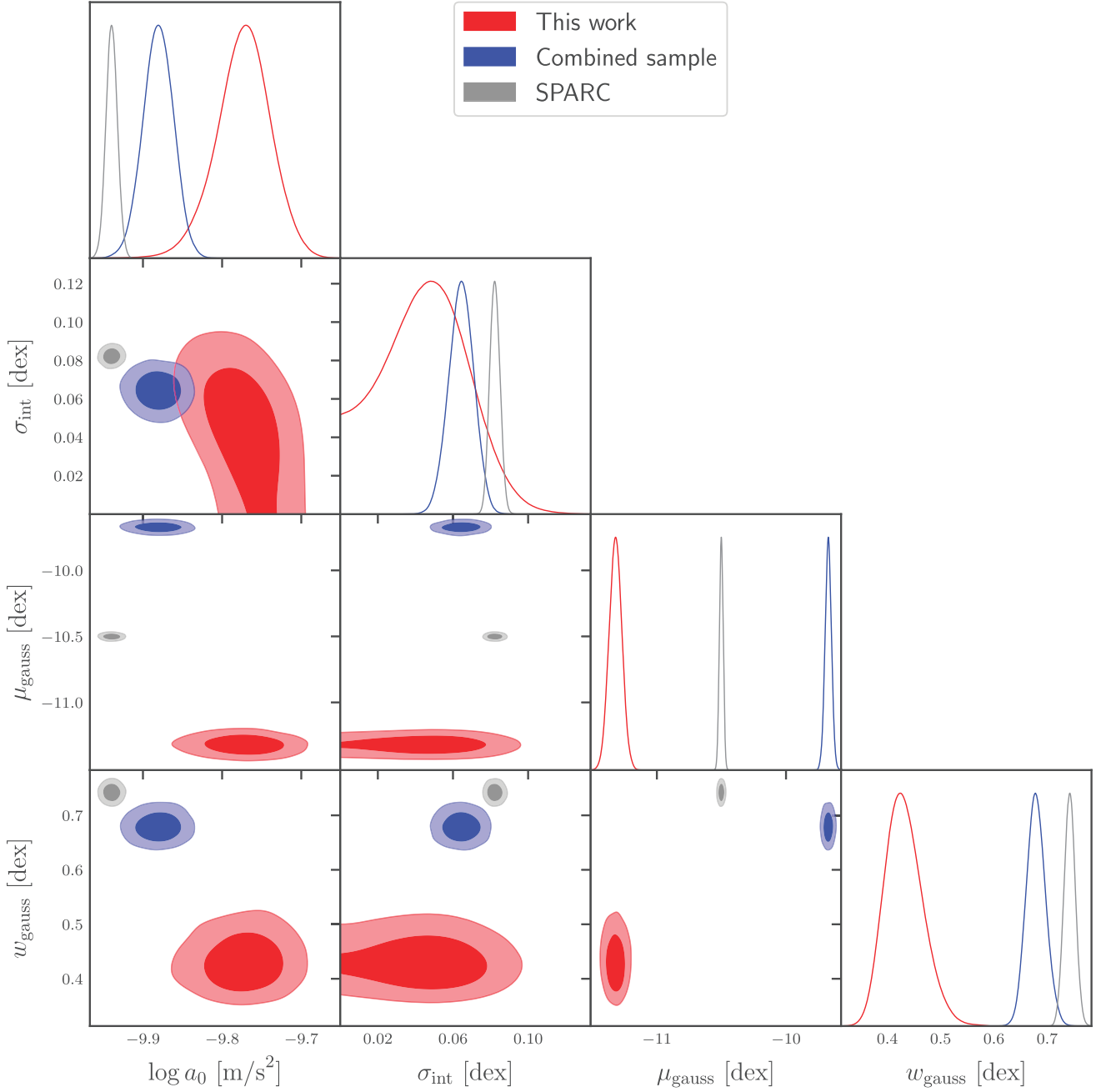**Figure B1.** The corner plot showing the posterior distribution of the parameters from the RAR sample fit for our sample in red, for the combined sample (this work + high acceleration portion of SPARC) in blue and all the SPARC data in grey. μ and w represent the mean and standard deviation of the Gaussian prior on the true $\log(g_{bar})$ values as implemented in the Marginalized Normal Regression method of ROXY.
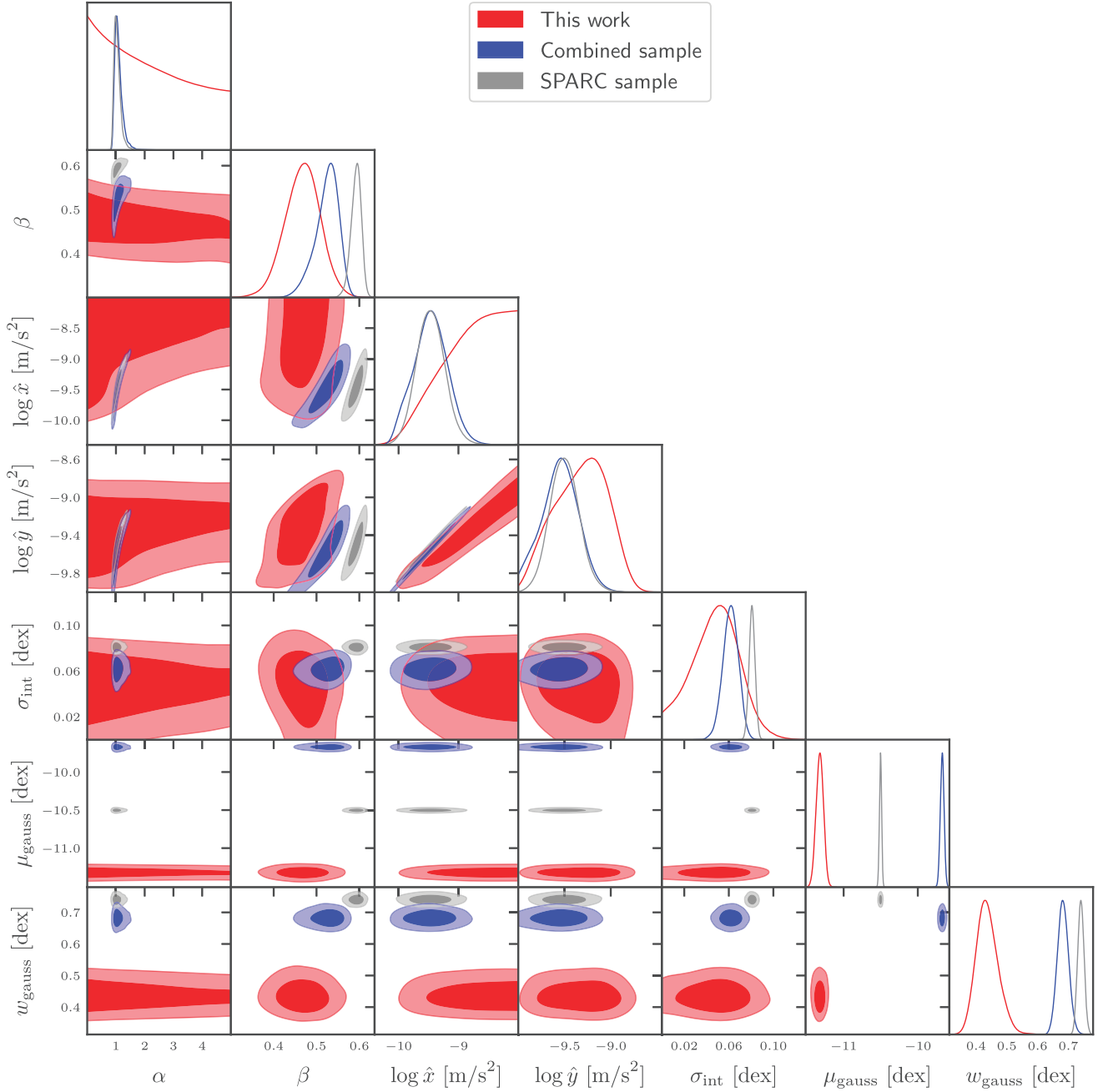
Figure B2. The corner plot showing the posterior distribution of the parameters for the double power law for our sample, the combined sample (this work + high acceleration portion of SPARC) and all the SPARC data.

Table B1. Table 4 but for the n and γ IF families.

IF family	Sample	MIGHTEE $\Upsilon_\star$	SPARC $\Upsilon_\star$	a_0	Shape	$\sigma_{\rm int}$
n	MIGHTEE	Varying Υ_K	–	2.02 ± 0.15	6.84 ± 3.05	0.040 ± 0.022
n	MIGHTEE	$\Upsilon_K = 0.6$	–	1.48 ± 0.095	9.19 ± 3.31	0.032 ± 0.019
n	SPARC	–	$\Upsilon_{\star,{\rm disc}} = 0.5, \Upsilon_{\star,{\rm bulge}} = 0.7$	1.04 ± 0.04	0.92 ± 0.03	0.081 ± 0.003
n	Low acceleration SPARC	–	$\Upsilon_{\star,{\rm disc}} = 0.5, \Upsilon_{\star,{\rm bulge}} = 0.7$	0.91 ± 0.05	0.81 ± 0.03	0.084 ± 0.003
n	MIGHTEE + high acceleration SPARC	Varying Υ_K	$\Upsilon_{\star,{\rm disc}} = 0.5, \Upsilon_{\star,{\rm bulge}} = 0.7$	1.82 ± 0.15	1.41 ± 0.11	0.061 ± 0.007
n	MIGHTEE + high acceleration SPARC	$\Upsilon_K = 0.6$	$\Upsilon_{\star,{\rm disc}} = 0.5, \Upsilon_{\star,{\rm bulge}} = 0.7$	1.33 ± 0.12	1.26 ± 0.09	0.047 ± 0.011
n	MIGHTEE + high acceleration SPARC discs	Varying Υ_K	$\Upsilon_\star = 0.27$	0.96 ± 0.21	0.54 ± 0.05	0.028 ± 0.017
γ	MIGHTEE	Varying Υ_K	–	1.65 ± 0.15	2.61 ± 1.42	0.045 ± 0.022
γ	MIGHTEE	$\Upsilon_K = 0.6$	–	1.13 ± 0.11	2.24 ± 0.98	0.051 ± 0.022
γ	SPARC	–	$\Upsilon_{\star,{\rm disc}} = 0.5, \Upsilon_{\star,{\rm bulge}} = 0.7$	0.97 ± 0.06	0.76 ± 0.05	0.081 ± 0.003
γ	Low acceleration SPARC	–	$\Upsilon_{\star,{\rm disc}} = 0.5, \Upsilon_{\star,{\rm bulge}} = 0.7$	0.78 ± 0.07	0.61 ± 0.04	0.084 ± 0.003
γ	MIGHTEE + high acceleration SPARC	Varying Υ_K	$\Upsilon_{\star,{\rm disc}} = 0.5, \Upsilon_{\star,{\rm bulge}} = 0.7$	1.57 ± 0.09	1.41 ± 0.16	0.063 ± 0.006
γ	MIGHTEE + high acceleration SPARC	$\Upsilon_\star = 0.6$	$\Upsilon_{\star,{\rm disc}} = 0.50, \Upsilon_{\star,{\rm bulge}} = 0.7$	1.19 ± 0.10	1.12 ± 0.11	0.051 ± 0.009
γ	MIGHTEE + high acceleration SPARC discs	Varying Υ_K	$\Upsilon_\star = 0.27$	1.19 ± 0.10	1.12 ± 0.11	0.051 ± 0.009

This paper has been typeset from a TeX/LaTeX file prepared by the author.